

Citric Juice-mediated Synthesis of Tellurium Nanoparticles with Antimicrobial and Anticancer Properties

David Medina Cruz^{1,†}, William Tien-Street^{1,2,†}, Bohan Zhang^{1,†}, Xinjing Huang^{1,†}, Ada Vernet Crua¹, Alfonso Nieto-Argüello³, Jorge L. Cholula-Díaz³, Lidia Martínez⁴, Yves Huttel⁴, María Ujué González⁵, José Miguel García-Martín⁵ and Thomas J. Webster^{1,*}

[†]*These authors contributed equally to this paper.*

¹ Department of Chemical Engineering, Northeastern University, Boston, MA 02115, USA

² Department of Bioengineering, Northeastern University, Boston, MA 02115, USA

³ School of Engineering and Sciences, Tecnológico de Monterrey, Av. Eugenio Garza Sada 2501, Monterrey, NL 64849, Mexico.

⁴ Materials Science Factory. Instituto de Ciencia de Materiales de Madrid, ICMN-CSIC, Sor Juana Inés de la Cruz 3, 28049 Madrid, Spain

⁵ Instituto de Micro y Nanotecnología, IMN-CNM, CSIC (CEI UAM+CSIC), Isaac Newton 8, 28760 Tres Cantos, Spain

*Correspondence: Thomas J. Webster

Department of Chemical Engineering, Northeastern University,

313 Snell Engineering Center, 360 Huntington Avenue, Boston, MA 02115

Tel +1 617 373 6585

Fax +1 617 373 2209; Email: th.webster@neu.edu

Abstract

Bacterial infections and cancer are two of the most significant concerns that the current healthcare system should tackle nowadays. Green nanotechnology is presented as a feasible solution that is able to produce materials with significant anticancer and antibacterial activity, while overcoming the main limitations of traditional synthesis. In the present work, orange, lemon and lime extracts were used as both reducing and capping agents for the green synthesis of tellurium nanoparticles (TeNPs) using a microwave-assisted reaction. TeNPs showed a uniform size distribution, and rod- and cubic-shapes, and were extensively characterized in terms of morphology, structure and composition using TEM, SEM, XPS, XRD, FTIR and EDX analysis. TeNPs showed an important antibacterial activity against both Gram-negative and -positive bacteria in a range concentrations from 5 to 50 $\mu\text{g/mL}$ over a 24-hour time period. Besides, nanoparticles showed anticancer effect towards human melanoma cells over 48 hours at concentrations up to 50 $\mu\text{g/mL}$. Moreover, the Te nanostructures showed no significant cytotoxic effect towards human dermal fibroblast at concentrations up to 50 $\mu\text{g/mL}$. Therefore, we present an environmentally-friendly and cost-effective synthesis of TeNPs using only fruit juices and showing enhanced and desirable biomedical properties towards both infectious diseases and cancer.

Keywords: Nanoparticle, Tellurium, Antimicrobial, Green-Synthesis, Bacteria, Anticancer, Citric

Introduction

The widespread use of antibiotics has led to the development of antibiotic-resistant bacteria, threatening our global healthcare system. Because of our over dependence and over prescription of antibiotics, humankind now lives in the post-antibiotic era, where diseases that were easily treated can now kill again^{1,2}. According to the Centers for Disease Control (CDC), antimicrobial-resistance to antibiotic (AMR) infections affect 2 million people in the United States annually, and it is predicted that more people will die from AMR pathologies than all diseases combined, including cancer, by 2050, culminating into one person dying from an infection every three seconds³.

Cancer, understood as the abnormal growth of cells and tissue within biological systems, is another socking concern that society should face where cancerous cells are also developing a resistance to commonly used chemotherapeutics. Using mechanisms such as drug target alteration, drug efflux, DNA damage repair and cell death inhibition, these resistant cells are not killed by conventional cancer therapies⁴. Data from the National Cancer Institute (NCI) shows that in 2018, an estimated 1.7 million new cases of cancer will be diagnosed in the United States and around 600,000 people will die from the disease⁵.

Nanotechnology emerged in the 1980s, and soon enough, it was applied to medicine, causing the birth of nanomedicine⁶. Since then, nanomedicine has been reported to decrease bacterial survival, cancerous cell activity and can simultaneously be compatible or even promote mammalian cell functions due to a combination of properties, especially depending on the interfacial layer of the nanoparticles^{7,8}. Nanoparticles fundamentally exhibit higher reactivity

compared to their respective bulk materials due to high surface area to volume ratios⁹. Moreover, due to their size, nanoparticles can penetrate bacterial and cancer cell membranes in a relatively simple way¹⁰. A wide variety of metallic nanoparticles that exhibit this behavior are composed of elements widely studied, including silver¹¹, gold¹², titanium and zinc oxides^{13,14}, silica¹⁵, and carbon¹⁶.

On the other hand, chalcogens, such as selenium (Se) and tellurium (Te) are gaining special interest in nanomedicine for biomedical applications^{17,18,19}. Previous research on the antibacterial properties of tellurium started as early as 1932, and the antimicrobial activity of the metalloid was even reported before the wide-spread use of antibiotics²⁰. Primarily, tunable tellurium nanoparticles (TeNPs) and nanotubes have been recently researched and produced for solar energy cells^{21,22}. In the biomedical field, tellurite ions (TeO_3^{2-}) have been previously researched and have long been known to be toxic and kill most Gram-negative bacteria at concentrations lower than other poisonous metals/metalloids^{23,24}.

Tellurium-based nanomaterials can be synthesized using different physical and chemical procedures²⁵. However, traditional chemical and physical synthesis methods can have significant drawbacks, including the use of high temperature and pressure, acidic pH of the medium, the use of harsh and expensive chemicals, and the formation toxic-by-products²⁶. For instance, some reducing agents used for the synthesis of nanomaterials, such as hydrazine or ammonia, represent a real concern not only for the laboratory in which they are used, but also for the environment²⁷. Besides, most of them are not accessible to research facilities in developing countries, where

antibacterial solutions are vitally needed to fight against the spread of bacteria that are resistant to antibiotics^{28,29}.

Therefore, new methods for nanoparticle synthesis are increasingly in demand to meet the need for clean, cost-effective, environmentally-friendly, and efficient synthesis processes³⁰. Compared to traditional synthesis approaches, green nanoparticles are clean, inexpensive, and utilize eco-friendly and non-toxic materials and methods³¹. The biological routes for nanoparticle synthesis can be relatively easy and performed in ambient conditions³². Living organisms (such as bacteria³³, fungi³⁴ and human cells³⁵) have shown the ability to reduce metallic ions to elemental nanoparticles. In addition, dietary compounds and natural components have been used, such as honey³⁶ or tea extracts³⁷.

Importantly during the green synthesis of nanoparticles, the biomolecules presented in the raw materials (such as proteins, cytokines, growth factors, ligands, etc.), may coat nanoparticles acting as natural stabilizers to prevent the formation of clusters of nanoparticles³⁸. Aggregation is an extremely detrimental property when discussing nanoparticles and their bioavailability within living organisms and can be a major drawback for the use of nanoparticles in medicine. When aggregated, nanomaterials lose their ability to, for instance, act as antibacterial or anticancer agents since they may not enter cells, clog membrane pores, or may even be cleared by the immune system if too large. Besides, more dispersed nanoparticles have a higher cytotoxic effect. The availability of the particles to be internalized by the cells seems to be strongly dependent on the size and morphology of the structures^{39,40}.

In this study, different citric juices are used as unique reducing and stabilizing agents for the formation of nanoparticles. On a molecular level, citric juices are composed of organic acids, sugars and phenolic compounds that are able to reduce metallic ions to their elemental form. While the main organic acids are citric, malic and ascorbic, the most important sugars are sucrose, glucose and fructose. Besides, there are between 10 and 15 phenolic compounds in these juices, including flavanones and hydroxycinnamic acids which can serve as reducing agents⁴¹⁻⁴³.

Therefore, we report the successful synthesis of TeNPs for the first time, using a green and environmentally-friendly approach employing citric extracts from the fruits as unique reducing and stabilizing agent. TeNPs with a uniform size distribution were synthesized using lemon (LEM-TeNPs), lime (LIM-TeNPs), and orange extract (OR-TeNPs). Once purified, a pioneer study of TeNPs made by green means was completed using extensive characterization in terms of composition and morphology and tested as antimicrobial agents against both antibiotic-resistant Gram-positive and Gram-negative bacteria, showing different degrees of bacterial inhibition. Furthermore, cytocompatibility tests were conducted to determine and quantify the effects of the nanoparticles on both healthy and cancerous human cells, showing no significant cytotoxicity for healthy cells yet promising anticancer activity at an acceptable concentration range.

Materials and Methods

Te nanoparticle synthesis and purification

For Te nanoparticle synthesis, a stock concentration of sodium tellurite (Na_2TeO_3) (Sigma Aldrich, St. Louis, MO) was prepared in deionized (DI) water. The different extracts were collected from fresh fruits (specifically, orange, lemon and lime) bought in a local supermarket. The fruits were squeezed, and the liquid was collected. Different metallic salt concentrations (100, 75, 50 and 25 mM) were added to a constant volume of the citric extract in a glass vial. Samples were named depending on the citric extracts used for the synthesis: orange-mediated (OR-TeNPs), lemon-mediated (LEM-TeNP) and lime-mediated (LIM-TeNPs) synthesis. Once mixed, a microwave-assisted reaction was followed. The vials were placed inside the microwave (Whirlpool WMC20005 YB) and a single cycle of heating at 750 W was completed for 10 s, followed by a cool-down of the reaction until reaching room temperature.

The purification process used was the following: the content of each one of the glass vials was transferred to a conical tube and centrifuged at 10,000 rpm for 30 min, generating a black pellet at the bottom of the tube. The solid was washed twice with DI and autoclaved water and the final solid was re-suspended in DI and autoclaved water inside a glass vial that was lyophilized for 24 h. The resulting black powder was weighed, and a specific amount of deionized and autoclaved water was added in order to obtain the desired concentration. The final suspension of Te nanostructures was stored in a fridge in the dark for further experiments.

The samples were centrifuged using both an Eppendorf™ Model 5430 Microcentrifuge and Eppendorf™ Model Centrifuge 5804 R, refrigerated, with Rotor A-4-44 incl. adapters for 15/50

mL conical tubes, a keypad, and at 230 V/50 – 60 Hz. A FreeZone Plus 2.5 Liter Cascade Console Freeze Dry System was used to lyophilize the samples and obtain the final powder. In addition, an ultrasonic homogenizer (model 150VT) with a power source of up to 150 W was used to homogenize the samples.

Characterization

Morphological characterization of the different nanomaterials was accomplished by transmission electron microscopy (TEM) using a JEM-1010 TEM (JEOL USA Inc., MA). To prepare samples for imaging, nanoparticles were dried on 300-mesh copper-coated carbon grids (Electron Microscopy Sciences, Hatfield, PA). A FEI Verios 460 Field Emission Microscope (FE-SEM) (FEI Europe B.V., Eindhoven, Netherlands) using selective secondary/backscattered electrons detection was also used for morphological characterization. For observation, 7 μ L of a solution of citric-TeNPs on DI water were deposited on clean Si substrates and were allowed to dry for more than 24 h. The images were taken with 2 kV acceleration voltage and a 25 pA electron beam current. Electron dispersive X-Ray spectroscopy (EDX) was performed using an EDX detector EDAX Octane Plus, Ametek B.V., Tilburg, Netherlands) coupled to the SEM previously mentioned, for the verification of the presence of elemental tellurium in the structures. SEM conditions for EDX measurements were 10 kV acceleration voltage and 400 pA beam current.

Structural analysis of the nanoparticles systems were carried out by infrared spectroscopy using a Fourier transform infrared spectrometer, Perkin Elmer 400 FT-IR/FT-NIR in attenuated total reflectance (ATR) mode. The samples for FT-IR analysis were prepared by drop casting the TeNPs colloids on a sample holder heated at ~ 50 °C. 5 mg were used to carry out the

measurement. The IR spectra were scanned in the range of 500 to 4000 cm^{-1} with a resolution of 4 cm^{-1} . The spectra were normalized, and the baseline corrected using Spectrum™ software from Perkin-Elmer.

Powder XRD patterns were obtained with a Rigaku MiniFlex 600 operating with a voltage of 40 kV, a current of 15 mA, and Cu-K α radiation ($\lambda = 1.542 \text{ \AA}$). All XRD patterns were recorded at room temperature with a step width of 0.05 (2θ) and scan speed of 0.2 $^{\circ}/\text{min}$. The preparation of the sample for XRD analysis was done by drying 8 mL of TeNPs colloids on the sample holder.

For X-Ray photoelectron spectroscopy (XPS) experiments, drops of the compounds dispersed in DI water were deposited on clean copper substrates for sample preparation. After water evaporation, the samples were loaded in a vacuum loadlock chamber and then transferred in the XPS Ultra High Vacuum chamber with a base pressure in the low of 10^{-10} mbar range. The XPS chamber was equipped with a hemispherical electron energy analyzer (SPECS Phoibos 100 spectrometer) and a Mg-K α (1253.6 eV) X-ray source. The angle between the hemispherical analyzer and the plane of the surface was kept at 60° . Wide scan spectra were recorded using an energy step of 0.5 eV and a pass-energy of 40 eV while specific core level spectra (Te 3d, O 1s and C 1s) were recorded using an energy step of 0.1 eV and a pass-energy of 20 eV. Data processing was performed with CasaXPS software (Casa software Ltd, Cheshire, UK). The absolute binding energies of the photoelectron spectra were determined by referencing to the Te 3d 5/2 metallic core level at 573 eV^{44,45}. The contributions of the MgK α satellite lines were subtracted and the spectra were normalized to the maximum intensity.

A SpectraMax M3 spectrophotometer (Molecular Devices, Sunnyvale, CA) was used to measure the optical density of the bacterial cultures. Growth curves and other bacterial analysis were performed in a plate reader SpectraMax® Paradigm® Multi-Mode Detection Platform.

For cell fixation studies, a Cressington 208HR High Resolution Sputter Coater and a Samdri®-PVT-3D Critical Point dryer was used to prepare the samples, that were imaged using a Hitachi S-4800 SEM instrument was used with a 3 kV accelerating voltage and 10 μ A beam current.

Stability analysis

In order to analyze the stability of the samples, TEM and Zeta-potential measurements were completed in fresh and 60-days old TeNPs synthesized using a Te-precursor solution concentration of 50 mM and the three different citric extracts.

Bacteria cultures

Multidrug-resistant (MDR) *Escherichia coli* (ATCC BAA-2471; ATCC, Manassas, VA) and Methicillin-resistant *Staphylococcus aureus* (MRSA) (ATCC 4330; ATCC, Manassas, VA) bacteria were selected for the antimicrobial tests to determine the effect of TeNPs synthesized with orange, lemon, and lime extracts. The cultures were maintained on agar plates at 4 °C. Bacteria were inoculated into 5 mL of sterile Tryptic Soy Broth (TSB, sigma) in a 50 mL Falcon conical centrifuge tube and incubated at 37 °C/200 rpm for 24 h. The optical density was then measured at 600 nm (OD_{600}) using a spectrophotometer. The overnight suspension was diluted to a final bacterial concentration of 10^6 colony forming units per milliliter (CFU/mL) prior to measuring the optical density.

Antimicrobial activity of TeNPs

The colony of each bacterial strain was re-suspended in TSB media. The bacterial suspension was placed in a shaking incubator to grow overnight at 200 rpm and remained at a constant 37 °C. The overnight suspension was diluted to a bacterial concentration of 10⁶ CFU/mL and a spectrophotometer was used to perform optical density measurements at 600 nm (OD₆₀₀). Moreover, the seeding density was determined in each experiment using a colony forming unit assay. Different concentrations of nanoparticles were mixed with 100 µL of bacteria in TSB medium and added to each well of a 96-well plate for the specific antimicrobial assay (Thermo Fisher Scientific, Waltham, MA). The control group consisted of bacteria mixed with 100 µL of TSB culture media without the presence of any Te nanoparticles. The final volume per each well was 200 µL. Once the plate was prepared, the absorbance values of all samples were measured at 600 nm every 2 min on the absorbance plate reader for 24 h. The values coming from the Te nanoparticles system were measured preparing negative controls made of nanoparticles and medium only. For the conversion of OD to CFU/mL, standard curves were used for each one of the bacteria.

The bacterial growth curves were obtained and fitted into the Gompertz model⁴⁶ by subtracting the initial values to the entire curve and shifting them to the starting point. For the application of Gompertz distribution, re-parametrization was needed in order to describe the biological parameters (A , μ , and λ) (Equation 2) rather than the mathematical ones (a , b , c ...) (Equation 1).

$$y = a * e^{-e^{(b-ct)}}$$

Equation 1. Gompertz equation in terms of mathematical parameters.

The Gompertz equation in terms of mathematical parameters was modified through a series of derivations to obtain the modified equation that was used for the fitting of the curves. The resulting equation describes a sigmoidal growth curve.

$$y = A \cdot e^{-e^{-\frac{\mu}{A}(\lambda-t)+1}}$$

Equation 2. Gompertz equation in terms of biological parameters.

Where the parameter y is related to the number of bacteria (corresponding to the optical density reading), A is the maximal possible value of y , μ is the maximal growth rate and λ is the lag time. The parameters A , μ and λ were estimated according to a least-squares estimation algorithm using a GRG nonlinear solver.

The colony counting assays were done by seeding the bacteria in a 96-well plated mixed with different concentrations of TeNPs. The plates were incubated at 37 °C during 8h and, after that period of time, the plates were removed from the incubator and diluted with PBS in a series of vials $\times 10^5$, $\times 10^6$ and $\times 10^7$. Three drops of 10 μ L were taken of each dilution and deposited in a TSB-Agar plate. After a final period of incubation of 8 h inside the incubator at 37 °C, the numbers of colonies formed were counted at the end of the incubation.

In vitro cytotoxicity assays with Te nanoparticles

Cytotoxicity assays were performed with primary human dermal fibroblasts (TCC® PCS-201-012TM, Manassas, VA) and melanoma (ATCC® CRL-1619, Manassas, VA) cells. Cells were cultured in Dulbecco's Modified Eagle Medium (DMEM; Thermo Fisher Scientific, Waltham, MA), supplemented with 10% fetal bovine serum (FBS; ATCC® 30-2020™, American Type Culture Collection, Manassas, VA) and 1% penicillin/streptomycin (Thermo Fisher Scientific,

Waltham, MA). MTS assays (CellTiter 96® AQueous One Solution Cell Proliferation Assay, Promega, Madison, WI) were carried out to assess cytotoxicity. Cells were seeded onto tissue-culture-treated 96-well plates (Thermo Fisher Scientific, Waltham, MA) at a final concentration of 5000 cells per well in 100 μ L of cell medium. After an incubation period of 24 h at 37 °C in a humidified incubator with 5% carbon dioxide (CO₂), the culture medium was replaced with 100 μ L of fresh cell medium containing concentrations from 5 to 100 μ g/mL of green-synthesized OR-TeNPs, LEM-TeNPs, and LIM-TeNPs. Cells were cultured for another 24 and 48 h at the same conditions and then washed with PBS, the medium was then replaced with 100 μ L of the MTS solution (prepared using a mixing ratio of 1:5 of MTS:medium). After the addition of the solution, the 96-well plate was incubated for 4 h in the incubator to allow for a color change. Then, the absorbance was measured at 490 nm on an absorbance plate reader (SpectraMAX M3, Molecular Devices) for cell viability after exposure to the TeNPs concentration. Cell viability was calculated by dividing the average absorbance obtained for each sample by the one achieved by the control sample, and then multiplied by 100. Controls containing cells and media, and just media, were also included in the 96-well plate to identify the normal growth of cells without nanoparticles and to determine the absorbance of the media itself.

Cell fixation and SEM imaging

Primary human dermal fibroblasts and melanoma cells were seeded in a 6-well plate with a glass coverslip (Fisher Brand) attached to the bottom. After an incubation period of 24 h at 37 °C in a humidified incubator with 5% carbon dioxide (CO₂), media was removed and replaced with fresh one containing a concentration of 50 μ g/mL of OR-, LEM- and LIM-TeNPs. Cells were cultured for another 24 h at same conditions. After, the coverslips were fixed with a primary fixative

solution containing 2.5% glutaraldehyde (Electron Microscopy Sciences, EMS) and 0.1 M sodium cacodylate buffer solution (Electron Microscopy Sciences, EMS) for 1 hour. Subsequently, the fixative solution was exchanged for 0.1 M sodium cacodylate buffer and the coverslips were washed 3 times for 10 min. Post-fixation was done using 1% osmium tetroxide (OsO₄) solution (Electron Microscopy Sciences, EMS) in buffer for 1 hour. Subsequently, the coverslips were washed three times with buffer and dehydration was progressively achieved with 35, 50, 70, 80, 95 and 100% ethanol (three times for the 100% ethanol). Finally, the coverslips were dried by liquid CO₂-ethanol exchange in a Samdri®-PVT-3D Critical Point dryer. The coverslips were mounted on SEM stubs with carbon adhesive tabs (Electron Microscopy Sciences, EMS) after treatment with liquid graphite, and then sputter coated with a thin layer of platinum using a Cressington 208HR High Resolution Sputter Coater. Digital images of the treated and untreated bacterial cells were acquired using a SEM microscope.

Reactive oxygen species (ROS) analysis of samples

For ROS quantification, 2',7'-dichlorodihydrofluorescein diacetate (H2DCFDA) was used. Human melanoma cells were seed in a 96 well-plate at a concentration of 5×10^4 cells/mL in presence of different concentrations of the TeNPs as well as in a control without any nanoparticles. The cell were cultured under standard culture conditions (37 °C in a humidified incubator with a 5% carbon dioxide (CO₂) atmosphere) for 24 h before the experiment. Briefly, the ROS indicator was reconstituted in anhydrous dimethylsulfoxide (DMSO) to make a concentrated stock solution that was kept and sealed. The growth media were then carefully removed and a fixed volume of the indicator in PBS was added to each one of the wells at a final concentration of 10 μM. The cells were incubated for 30 min as optimal temperature and the

loading buffer was removed after. Fresh media were added and cells were allowed to recover for a short time. The baseline for fluorescence intensity of a sample of the loaded cell period exposure was determined. Positive controls were done stimulating the oxidative activity with hydrogen peroxide to a final concentration of 50 μM . The intensity of fluorescence was then observed by flow cytometry. Measurements were taken by an increase in fluorescence at 530 nm when the sample was excited at 485 nm. Fluorescence was also determined in the negative control—untreated loaded with dye cells maintained in a buffer.

Statistical analysis

All experiments were repeated in triplicate ($N = 3$) to ensure reliability of results. Statistical significance was assessed using student's t-tests, with a $p < 0.05$ being statistically significant. Results are displayed as mean \pm standard deviation.

Results and Discussion

Synthesis and purification of TeNPs

A facile and quick synthesis of TeNPs using orange, lemon and lime extracts was successfully completed, showing the ability of the extracts as both reducing and stabilizing agents for the generation of elemental tellurium-based nanomaterials. The reduction of Te from ionic state (Te^{4+}) to elemental form (Te^0) is achieved with the appearance of a dark color within the solution. A change of color from light to dark yellow was observed for all the Te-precursor solution concentrations after a few seconds of reaction (Figure S1 in Supplementary information). However, there was no noticeable difference in tone between the different citric extracts.

Therefore, a green and cost-effective approach can be achieved using the microwave-assisted method. The reduction of metallic ions within the solution of nanomaterials is only accomplished in the presence of both reducing and stabilizing agents⁴⁷. Thus, these agents must be present in the reaction and come from the juice extracts.

Characterization of the Te nanoparticles

After purification, the synthesized TeNPs using different Te-precursor solution concentrations and citric extracts were characterized by TEM in terms of size and morphology with the aim to understand the effect of the extracts (Figures S2, S3 and S4 in Supplementary information). TEM images show that, for all metallic salt concentrations, there is no difference regarding these two properties. Therefore, for the following characterization and further experiments, a concentration of 50 mM of metallic salt has been chosen (see Supplementary information for other concentrations).

TEM images (see Figure 1) showed that the nanostructures synthesized by different extracts had different morphology and shape. Thin nanorods with both sharp ends were found for OR-TeNPs, with around 50-200 nm in length and a 2-15 nm wide (Figure 1A). LEM- and LIM-TeNPs yielded a mixture of cubic-shaped nanoparticles with 100-200 nm in length (Figures 1B and 1C, respectively).

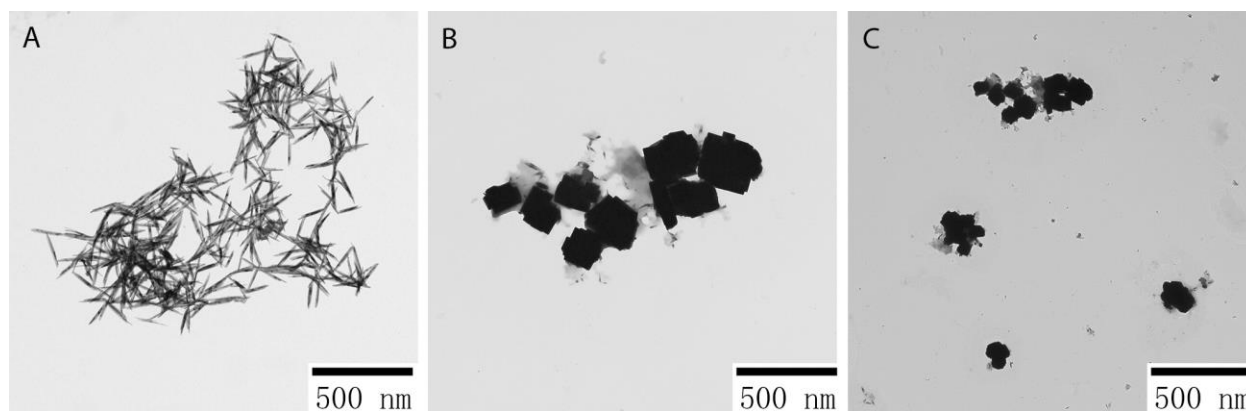


Figure 1. Transmission electron microscopy (TEM) characterization of TeNPs synthesized by orange (A), lemon (B) and lime (C) juices with 50 mM of metallic salt concentration. Different morphologies and features were found when the nanomaterials were characterized by TEM.

The only effect of the metallic salt precursor concentration, as determined by TEM, is that larger concentration leads to the formation of bigger and more numerous aggregates of nanoparticles (Figures S2, S3 and S4).

SEM characterization on OR-TeNPs (Figure 2A) showed a homogeneous rod structure while for the LEM-TeNPs (Figure 2B) and LIM-TeNPs (Figure 2C), cubic-shaped structures were clearly observed. Importantly, a non-metallic organic matrix was observed surrounding the nanoparticles for all samples. The presence of the organic coating embedding the cubes for LEM- and LIM-samples made difficult the observation of very small nanoparticles together with the bigger structures in standard conditions, i.e. imaging with secondary electrons. However, when the images are obtained using back-scattered electrons, whose signal depends on the atomic number Z , structures composed of Te ($Z=52$) can also be distinguished with brighter contrast than the organic coating ($Z=6$ and 8 for C and O, respectively). For instance, Figures 2D-2F show

representative back-scattered electrons images of OR-, LEM- and LIM-TeNPs. Only Te nanorods are seen in the OR-TeNPs sample, in agreement with the TEM characterization, while for the LEM- and LIM- samples both big crystal cubes and very small nanoparticles (around 10 nm size) immersed in the organic matrix can be observed. For the LEM-TeNPs sample, some nanorods can be discerned too.

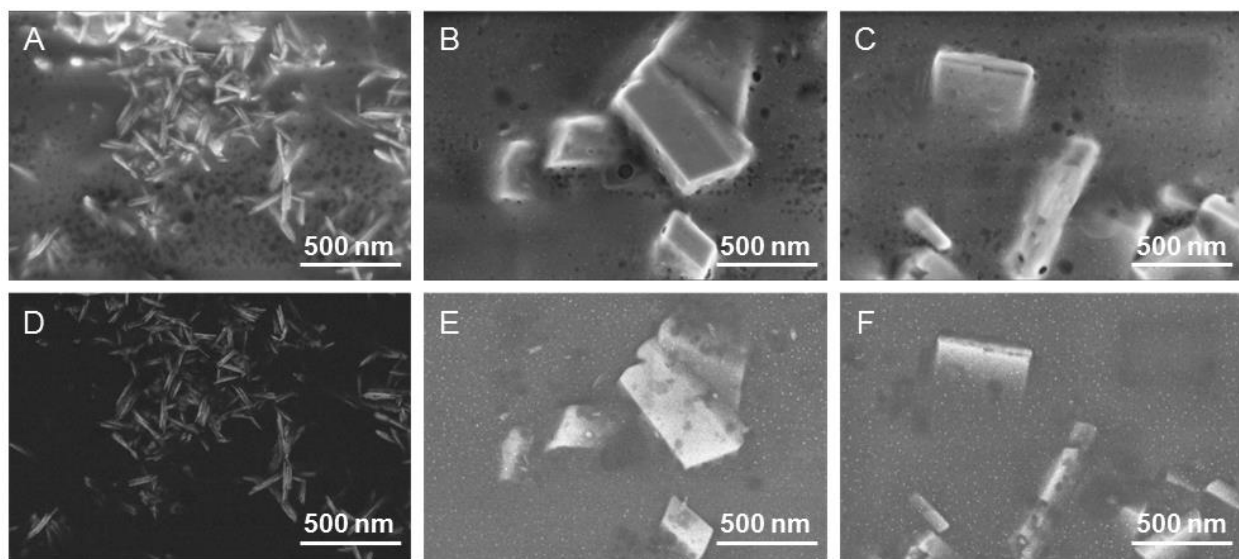


Figure 2. Scanning Electron Microscopy (SEM) image of OR-TeNPs (A, D), LEM-TeNPs (B, E) and LIM-TeNPs (C, F). The characteristic morphology of the nanostructures was observed using SEM. The upper images (A-C) correspond to secondary electrons micrographs and show the morphology of the obtained structures, while the lower ones (D-F) are taken with back-scattered electrons and provide compositional contrast. The scale bar is the same for all images (500 nm).

To determine the elemental composition and structure of the Te nanostructures, EDX, XRD and XPS measurements were performed. EDX characterization confirmed that the electron-dense structures were composed of tellurium as proven by the presence of specific tellurium peaks in all samples (Figures S5, S6 and S7 in Supplementary information). Besides, significant peaks for carbon and oxygen were found, as well as sodium, indicating the presence of an organic coating and reaction products surrounding the nanostructures. However, it was difficult to determine if

these peaks come either from the embedding matrix or from inside the rods and cubes. Summarizing, both SEM and EDX characterization allowed determining that in LEM- and LIM-samples both cubic crystals and small particles containing tellurium coexist, while in OR-samples no cubes but well-formed Te nanorods were observed.

XRD patterns are shown in Figure 3. The diffraction peaks for the OR-TeNPs XRD pattern (Figure 3a) can be indexed to the hexagonal Te structure (*h*-Te, space group $P3_121$)⁴⁸. The XRD analysis indicated the presence of foreign phases, probably tetraoxotelluric acid and/or telluric oxide (the diffraction peaks appeared at diffraction angles $2\theta < 20^\circ$, not shown in Figure 3). The lattice parameters calculated for the hexagonal OR-TeNPs are in good agreement with the reported values for *h*-Te⁴⁸, as shown in Table S1. In the case of the XRD analysis of LEM-TeNPs and LIM-TeNPs (Figure 3c and d) both XRD patterns can be indexed to orthorhombic β -TeO₂ (space group $Pbca$)⁴⁹. The diffraction peak at $2\theta \approx 25.7^\circ$ may correspond to the crystallographic plane (110) of tetragonal α -TeO₂ (space group $P4_32_12$)⁵⁰. The lattice parameters calculated for the orthorhombic LEM-TeNPs and LIM-TeNPs are also reported in Table S1 in Supplementary information.

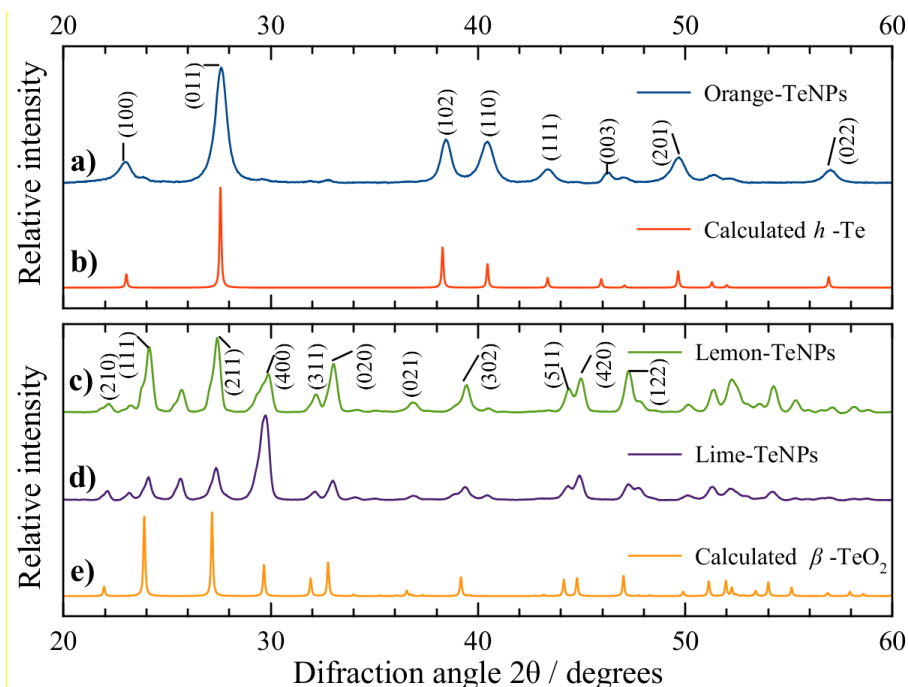


Figure 3. Comparison between the experimental XRD patterns for (a) OR-TeNPs, (c) LEM-TeNPs and (d) LIM-TeNPs with the calculated XRD patterns for (b) bulk hexagonal Te (h -Te)⁴⁸ and (e) orthorhombic β -TeO₂⁴⁹. Upper panel: Miller indices for h -Te. Lower panel: Miller indices for β -TeO₂.

XPS was used to characterize the chemical composition and electronic states of the different Te nanomaterials. Figure 4 presents the wide energy range scan of the Te nanoparticles obtained from the orange, lime and lemon juices. As seen, the three samples present the same elements. Apart from the tellurium, carbon, oxygen, nitrogen and sodium were detected. Copper from the substrate was also detectable, but not considered in the quantification depicted in Table S2 in Supplementary information. A comparison of the three samples evidenced that the highest Te concentration was detected in the lemon dispersion, which doubled the orange one. A detailed analysis of the core level peaks enabled the observation of certain differences between the samples, as shown in Figure S8 and values from Table S3 in Supplementary information.

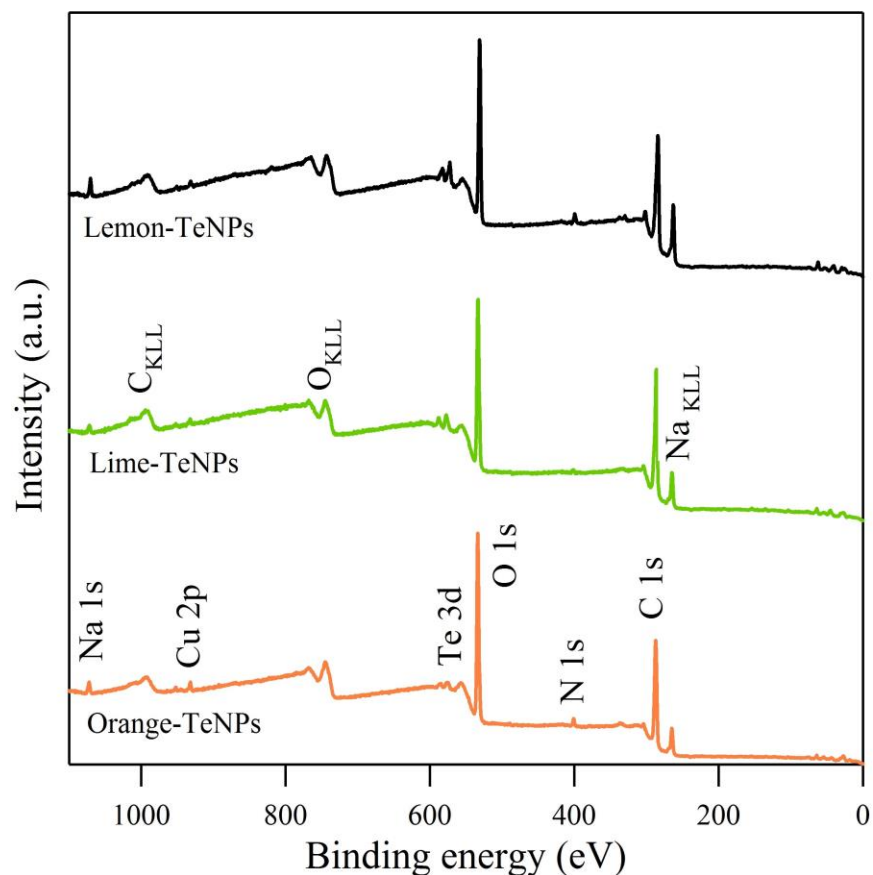


Figure 4. XPS wide scan of Te nanostructures obtained from orange, lime and lemon extracts.

FT-IR spectroscopy measurements were completed in order to identify the capping agents in the Te nanoparticles. The FT-IR spectra of OR-, LEM- and LIM-TeNPs are shown in Figure 5. The signals found in each of the IR spectra correspond to the most representative functional groups found in the juice from the rag and pulp of citrus fruits, *i.e.*, sugars (e.g. sucrose, glucose, and fructose), flavonoids (e.g. hesperidin) and water-soluble pectin molecules (e.g. protopectin, calcium and magnesium pectates)⁵¹⁻⁵⁴. For all of the FT-IR spectra, the bands are assigned to the antisymmetric stretching vibration of -OH, -CH₃ and -CH₂ at 3284, 2918 and 2840 cm⁻¹, respectively. The signal at 1634 cm⁻¹ was associated to the deformation vibrations of water in the sample. The signals within the region of 800-1500 cm⁻¹ were due to the deformation vibrations

of O–H and C–H bonds of pyranose rings. The peak at 1042 cm^{-1} was assigned to the vibration absorption of C–O⁵⁵. In the case of LEM–TeNPs and LIM–TeNPs, medium absorption bands due to tellurium dioxide (TeO_2) around 720 and 564 cm^{-1} were observed, while in OR–TeNPs only weak signals at same regions were identified, which may correspond to the presence of TeO_2 in the sample⁵⁶. These two bands are related to the symmetrical equatorial and asymmetrical axial stretching vibrations of the Te–O bonds, respectively⁵⁷.

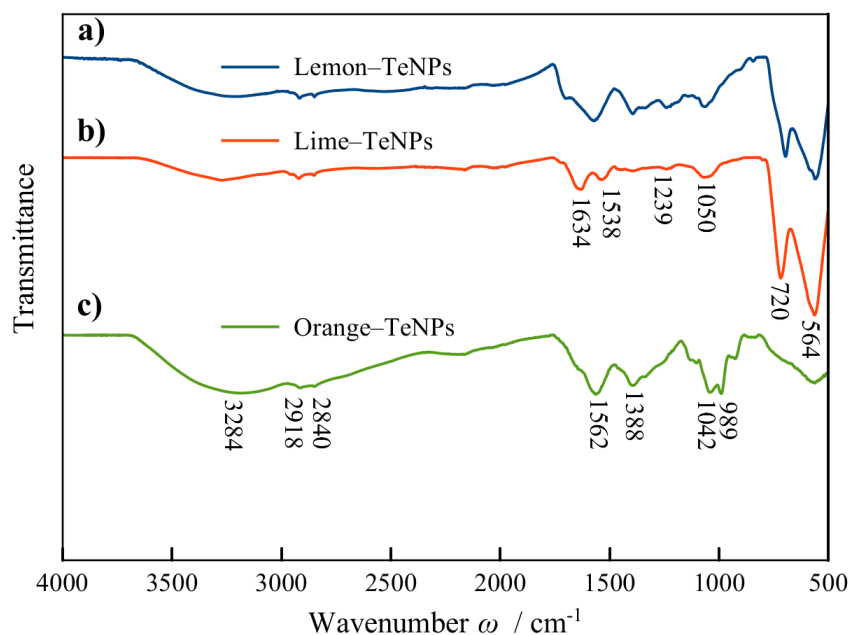


Figure 5. FT-IR spectra of (a) LEM–TeNPs, (b) LIM–TeNPs and (c) OR–TeNPs.

Stability analysis of the TeNPs after 60-days of their synthesis (using 50 mM Te-precursor solution concentration) by TEM imaging (Figure S9 in Supplementary information) and Zeta-potential measurements (Table S4 in Supplementary information) was completed. In both cases, the aged samples kept their original features.

Antimicrobial activity of TeNPs

The antimicrobial activity of the nanostructures was tested against two different bacterial strains, MDR-*Escherichia coli* and MRSA in order to evaluate their antibacterial potential against both Gram-negative and -positive bacteria, respectively. Experiments using 24 h growth curves (Figure S10 in Supplementary information) showed a promising antibacterial effect in a range of nanoparticle concentrations between 5 and 50 $\mu\text{g/mL}$ due to a decrease and inhibition in bacterial growth for both strains. This decay seemed to increase with a rise in concentration.

When OR-TeNPs were added to a culture of MDR-*Escherichia coli*, significant bacterial inhibition was found for the whole range of concentrations (Figures S10A in Supplementary information), while for LEM-TeNPs and LIM-TeNPs, the antimicrobial effect was slightly less significant (Figures S10C and S10E in Supplementary information, respectively). No significant inhibition was found for the minimum concentration (5 $\mu\text{g/mL}$) for both cases, with dose-dependent trend in bacterial inhibition. For MRSA experiments, OR-TeNPs showed again the highest antimicrobial effect compared to the other nanosystems, with an important impact in the bacterial cell proliferation over time (Figure S10B in Supplementary information). LEM-TeNPs and LIM-TeNPs showed a slight impact on the growth, with higher TeNPs concentrations meaning an increased antimicrobial effect for lemon-mediated Te nanoparticles (Figure S10D in Supplementary information), but no significant change for the lime-mediated Te nanostructures (Figure S10F in Supplementary information). The dose-dependent antibacterial effect on both bacterial strains was confirmed after modelization of the growth curves with Gompertz analysis (Figure S11 in Supplementary information).

Colony forming unit assays were also performed to assess the interaction between the synthesized TeNPs and the bacterial strains MDR-*Escherichia coli* and MRSA. When MDR-*Escherichia coli* was grown with OR-TeNPs (Figure 6A), a significant inhibition effect over the cell proliferation was found, with a similar activity of all the Te nanoparticle concentrations, achieving a 50% inhibition compared to the control. For LEM-TeNPs (Figure 6C), no significant inhibition was found for lower concentrations, while higher than 15 µg/mL caused an inhibition above 50%. Similar situation was found for LIM-TeNPs (Figure 6D), where Te nanoparticle concentrations over 10 µg/mL showed an important inhibition of the bacterial proliferation.

Experiments with MRSA showed a significant inhibition effect with a constant trend when OR-TeNPs were present in the bacterial culture (Figure 6B), while no significant inhibition (or not at all) was found for lower concentrations of LEM-TeNPs (Figure 6D) and LIM-TeNPs (Figure 6F). Only concentrations over 15 µg/mL seemed to develop a slight antimicrobial effect for both nanomaterials.

Consequently, OR-TeNPs seem to have the most important antimicrobial effect over both bacterial strains, with inhibition of the bacterial population over 50% for most of the TeNPs concentrations. This effect is especially noticeable for MDR-*Escherichia coli*, closely followed by the gram-positive bacteria. However, no significant antibacterial effect was found when LEM- and LIM-TeNPs were cultured with MRSA, while showing an important inhibition for MDR-*Escherichia coli*. Overall, all the Te nanoparticles have better antimicrobial properties against Gram-negative bacteria.

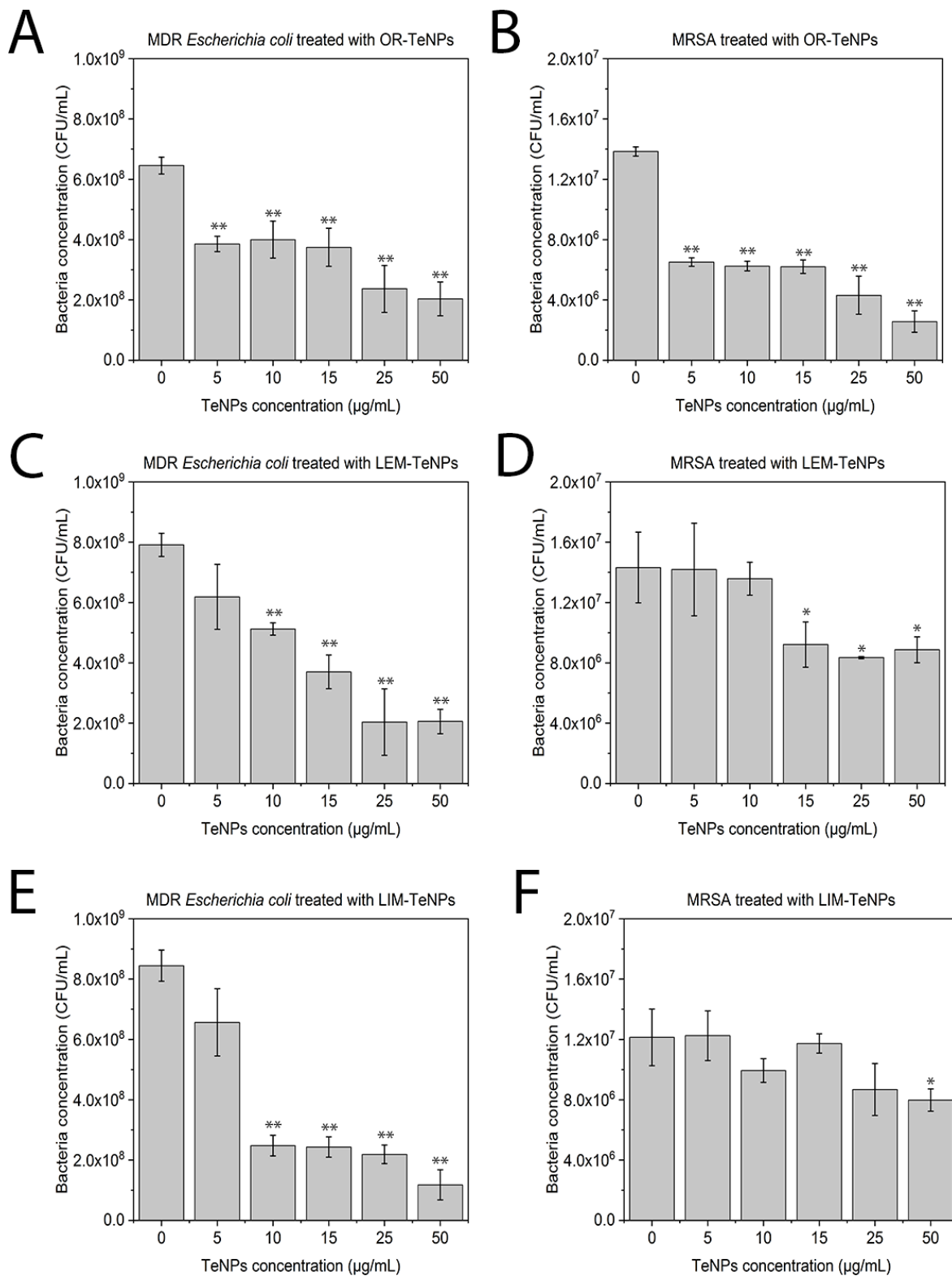


Figure 6. Colony counting assay of MDR-*Escherichia coli* (A, C, E) and Methicillin-resistant *Staphylococcus aureus*, MRSA (B, D, F) after being treated for 8 h with different citrics-mediated synthesized nanoparticles. Data = mean +/- SEM, N=3. * $p < 0.05$ versus control (0 µg/mL concentration), ** $p < 0.01$ versus control (0 µg/mL concentration).

IC₅₀ values were obtained with the aim to show the minimum inhibitory concentration for each one of the bacterial tests (Table 1).

Table 1. IC₅₀ values (in µg/mL) for different Te nanoparticles against MDR-*Escherichia coli* and MRSA.
Error values are given for each one of the parameters.

Te-nanosystems	MDR-<i>Escherichia coli</i>	MRSA
OR-TeNPs	21.38 ±3.06	21.98 ±3.96
LEM-TeNPs	8.18 ±1.25	33.51 ±9.59
LIM-TeNPs	6.23 ±0.92	34.68 ±8.12

These values differ from others found in literature, showing a decrease of the IC₅₀ values for our Te nanosystems. For example, Zare et al.⁵⁸ have investigated the antibacterial effect of Te nanorods (TeNRs) using Minimum Inhibitory Concentration (MIC) as quantifying values. The TeNRs, produced by the *Bacillus sp. BZ* were tested against *Staphylococcus aureus* (MIC 250 µg/mL), *P. aeruginosa* (MIC 125 µg/mL), *S. typhi* (MIC µg/mL), and *K. pneumonia* (MIC 125 µg/mL).

The bactericidal effect of Te nanoparticles has been studied¹⁹, and it can be related to the production of reactive oxygen species (ROS) upon exposure of the bacterial cultures. Besides, evidence so far suggests that the antimicrobial activity seems to be directly linked to the dimensions of the nanoparticles: indeed, the highest activity was shown by nanoparticles of smaller sizes. As nanoparticles decrease in size, their surface to volume ratio increase, confirming smaller is better for improving the biological reactivity. Nevertheless, size is not the sole parameter influencing antimicrobial properties of the nanoparticles: other important features

are both the elemental composition and the shape⁵⁹. Besides, it is hypothesized that the presence of the natural coating surrounding the nanoparticles can have an important effect of the biomedical properties.

Moreover, tellurium oxyanions have also been found to trigger the generation of ROS, with both elements capable of reacting with intracellular thiols and forming intermediates that cause oxidative stress because of the formation of superoxide radicals⁶⁰. Thus, even if reactive oxygen species are involved in the toxicity of TeNPs, other mechanisms may be responsible for the antimicrobial activity of these nanostructured metals. For instance, it seems that Te nanoparticles can contribute to functional damages of cell membrane or wall by disrupting the integrity of these important envelopes⁶¹. Some other mechanism related to the surface features of the nanoparticles may be involved, however, in conferring toxicity to TeNPs. For instance, the presence of a natural and organic-based coating surrounding the nanoparticles can be closely related to the enhancement of the bacterial activity towards other nanoparticles systems.

In vitro cytocompatibility and cytotoxicity of TeNPs with healthy and cancer cells

With the aim to determine the cytotoxicity associated with the green-synthesized TeNPs in mammalian cells, *in vitro* cytotoxicity assays were performed with human dermal fibroblasts (HDF) and human melanoma cells for 24 and 48 h. Experiments with fibroblast cells showed a decrease in the cell viability with a Te nanoparticle concentration increase for all the systems, with a constant cell proliferation after 48 h of growth. OR-TeNPs (Figure 7A) remained cytocompatible (with cell growth over 60%) for concentrations up to 50 µg/mL for both experimental days while an important depletion of the cell proliferation was found at

concentrations higher than 25 $\mu\text{g}/\text{mL}$ and 10 $\mu\text{g}/\text{mL}$ for LEM-TeNPs (Figure 7B) and LIM-TeNPs (Figure 7C), respectively.

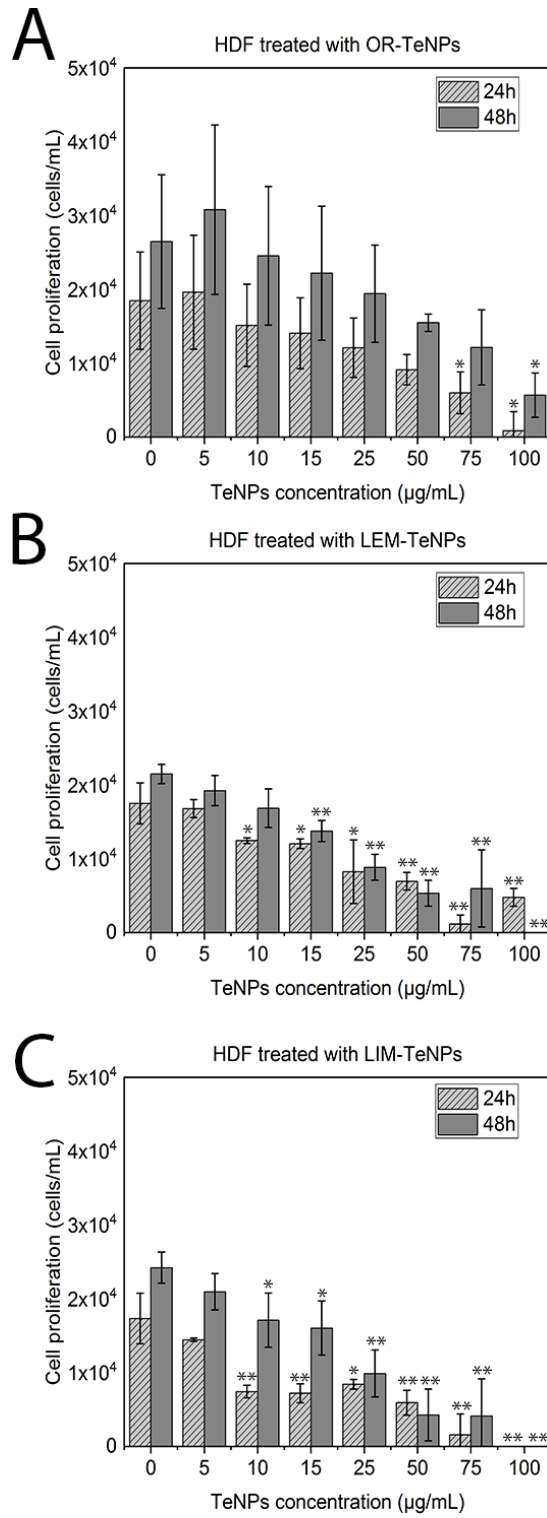


Figure 7. MTS assay on human dermal fibroblast (HDF) in the presence of OR-TeNPs (A), LEM-TeNPs (B) and LIM-TeNPs (C) ranging from 5 to 100 $\mu\text{g}/\text{mL}$. Data = mean \pm SEM, N = 3. * $p < 0.05$ versus control (0 $\mu\text{g}/\text{mL}$ concentration), ** $p < 0.01$ versus control (0 $\mu\text{g}/\text{mL}$ concentration)

The second set of experiments was carried out with cancerous melanoma cells were used to evaluate the potential anticancer effect of the Te nanoparticles (Figure 8). TeNPs concentrations from 5 to 100 $\mu\text{g/mL}$ were tested in all the different nanosystems with the objective of observing the potential biomedical application of the nanoparticles.

OR-TeNPs (Figure 8A) showed inhibition of cell growth in the extended range of concentrations, nevertheless, it was accentuated at concentrations higher than 25 $\mu\text{g/mL}$. With similar behavior, LEM-TeNPs (Figure 8B) presented an increasing decrease in cell proliferation. Lower TeNPs concentrations of 10 and 25 $\mu\text{g/mL}$ showed a specifically remarkable recession, therefore confirming that even a lower density of Te nanoparticles produced significant anticancer activity in comparison to the normal growth of the cells (presented in the graph as 0 $\mu\text{g/mL}$ columns). Finally, LIM-TeNPs (Figure 8C) presented a different tendency in comparison to the others citric juices. Lower concentrations of metallic nanoparticles seemed to produce a non-notable delay on the cell proliferation, however, 50 $\mu\text{g/mL}$ and greater concentrations of TeNPs showed a sharp decrease juxtaposed with the control rise. Consequently, according with these results, it can be concluded that in average, the anticancer effect presented in these Te nanostructures is enhanced at higher nanoparticle concentrations. Nonetheless, low concentrations of LIM-TeNPs present also a good performance, allowing the use of these biogenic nanoparticles for biomedical applications with no cytotoxic effect associated.

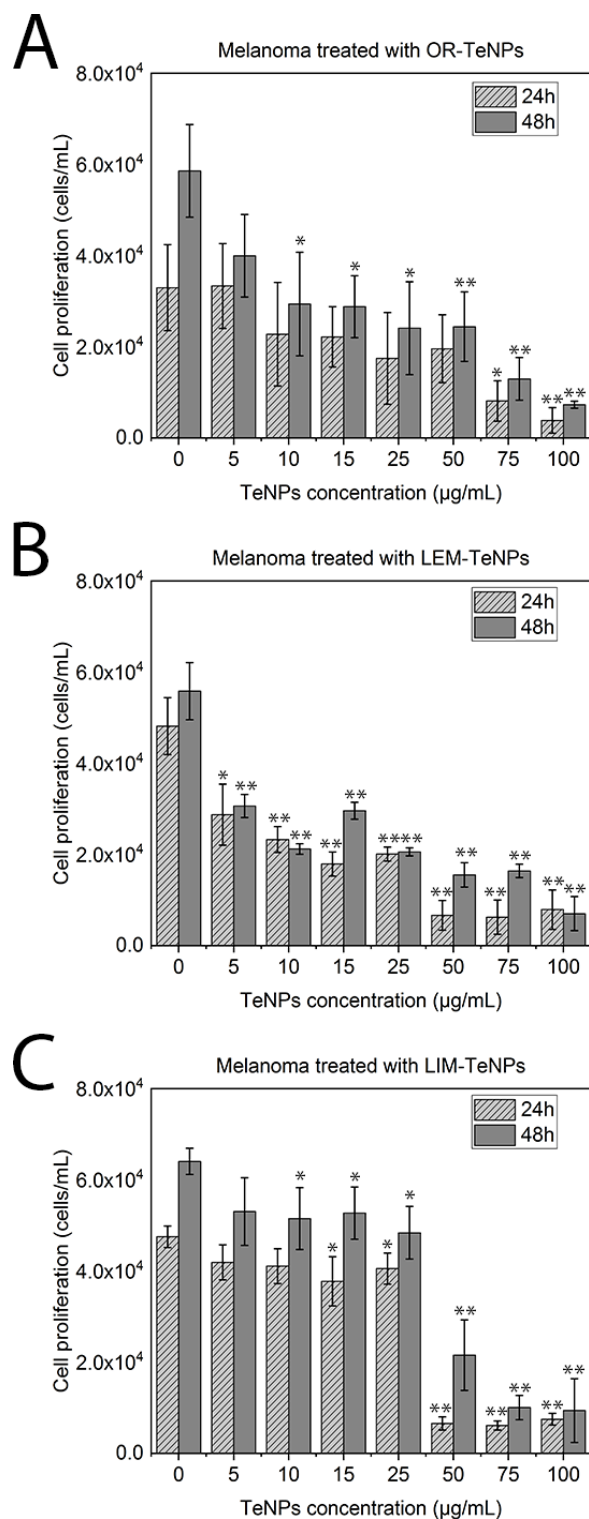


Figure 8. MTS assay on human melanoma cells in the presence of OR-TeNPs (A), LEM-TeNPs (B) and LIM-TeNPs (C) ranging from 5 to 100 µg/mL. Data = mean +/- SEM, N = 3. *p < 0.05 versus control (0 µg/mL concentration), **p < 0.01 versus control (0 µg/mL concentration).

The cytotoxic effect on both cell lines was evaluated, showing a dose-dependent cytotoxic effect over the cells after 48 h of experiments (Figure 9). The Te nanoparticles caused a decrease in the proliferation of cells for both healthy and cancer cell lines. However, the decay is more pronounced for cancer cells (Figure 9B), showing higher cytotoxicity. OR-TeNPs showed the best cytocompatibility towards HDF cells, with a significant cytotoxic effect on melanoma cells over the whole range of Te nanoparticle concentrations (Figure 9A). LEM- and LIM-TeNPs showed a similar trend when exposed to HDF cells, while the cytotoxic effect on melanoma cells was not so pronounced for LIM-TeNPs as it was for LEM-TeNPs, which shows a similar effect on cell proliferation as OR-TeNPs (even better at low concentrations).

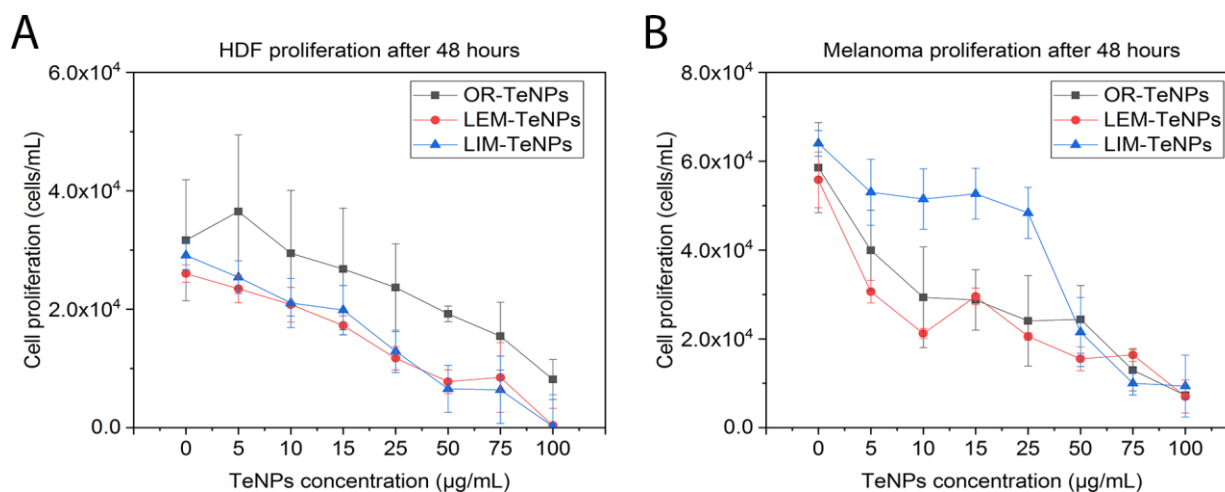


Figure 9. MTS assay on HDF (A) and melanoma (B) cells in the presence of OR-, LEM- and LIM-TeNPs ranging from 5 to 100 µg/mL after 48 h of experiment. Data = mean +/- SEM, N = 3.

Overall, results from this part of the study showed for the first time that citric-derived TeNPs displayed both antibacterial and anticancer effects and a negligible cytotoxic effect for human healthy cells within an ideal range from 5 to 50 µg/mL.

Reactive oxygen species (ROS) analysis

ROS analysis (Figure 10) showed an increase in the ROS production when nanoparticles were present in the media, with a dose-dependent effect. Therefore, the increase in the number of reactive oxygen species is related to the dose-dependent anticancer behavior that was shown before.

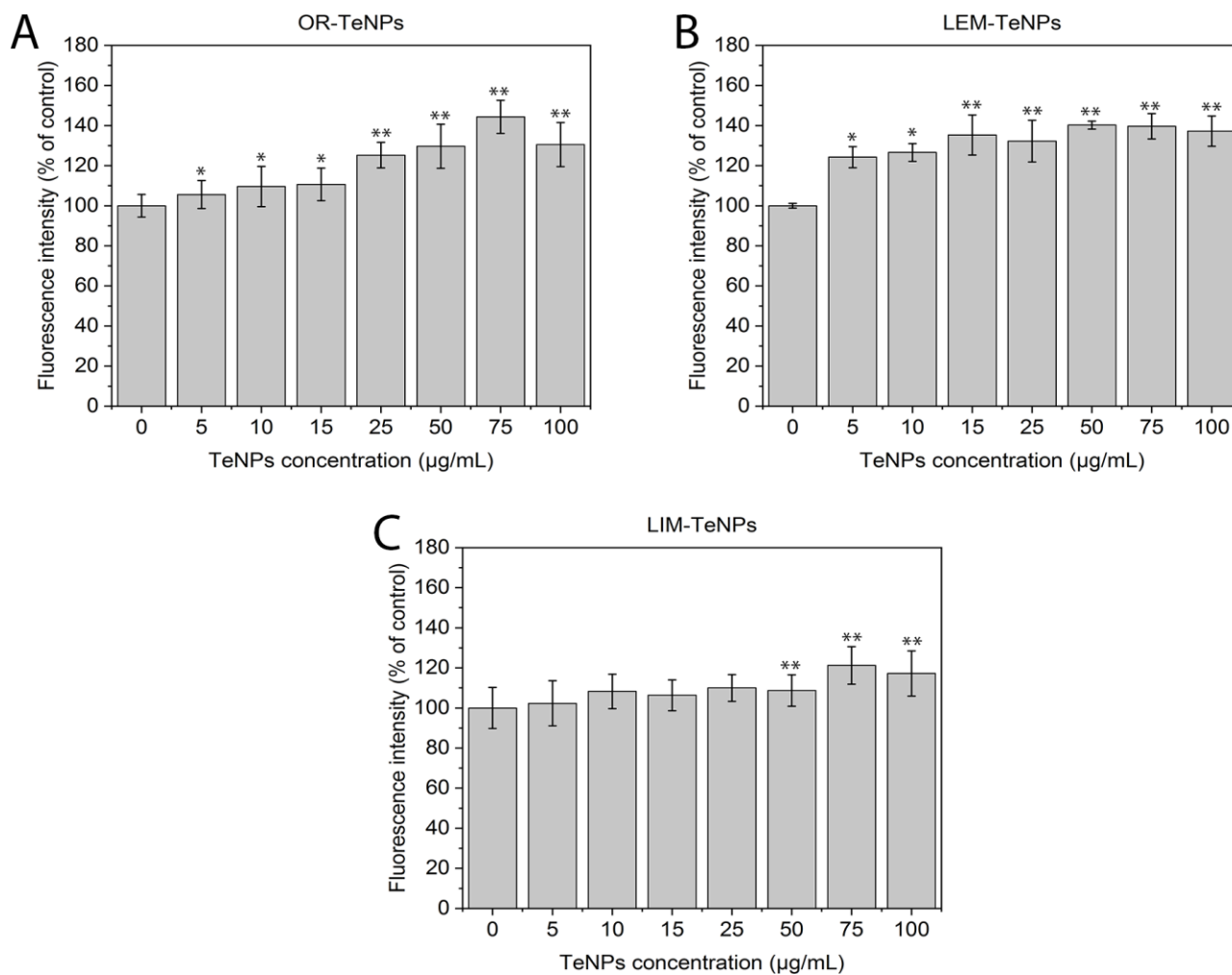


Figure 10. Reactive Oxygen Species (ROS) analysis. The ROS production has been evaluated for the different nanoparticles (OR-, LEM- and LIM-TeNPs) in experiments with Human Melanoma cells (A, B, C). Data = mean \pm SEM, $N=3$. * $p < 0.05$ versus control (0 $\mu\text{g/mL}$ concentration), ** $p < 0.01$ versus control (0 $\mu\text{g/mL}$ concentration).

It was hypothesized that the cytocompatibility of the Te nanostructures was associated to the organic coating present all over the Te nanostructures. This coating (composed of organic material from the synthesis) surrounding the Te surface would prevent from the ions release and finally avoid cell damage. Several studies have shown an enhancement of cytocompatibility of green-synthesized nanoparticles in comparison to chemically-synthesized nanoparticles, showing no significant cytotoxic effect on the cells^{62,63}.

A deteriorate ROS protective mechanisms is found in cancer cells, what explain the anticancer effect. Several studies have reported the anticancer effect of Te compounds⁶⁴, but only a few, if any, studies have shown this activity in tellurium nanomaterials⁶⁵. After synthesis, some molecules remained in the coating surrounding the surface of the nanoparticles (such as citric acid and vitamin C). Both compounds are known to have anticancer properties^{66,67}. Thus, it is strongly believed that the synergetic effects of both metallic core and coating enhance the anticancer properties thus, presenting citric-TeNPs as a novel solution for anticancer activity with low associated cytotoxicity towards healthy cells. The anticancer effect of these citric TeNPs may also be attributed to the generation of ROS, since Te nanoparticles have been reported as strong agents for ROS-mediated apoptosis and genotoxicity⁶⁸.

IC₅₀ values were calculated for the anticancer effect of the nanoparticles, rendering 0.204, 0.135 and 0.039 mg/mL for OR-, LEM- and LIM-TeNPs, respectively. Therefore, it is possible to compare in terms of efficacy to other metallic nanosystems reported in literature. For instance, Hafeez et al. studied dacarbazine laden nanoparticle (DZNP) and dacarbazine laden nanocream (DZNC) topical delivery system for the treatment of melanoma⁶⁹. Dacarbazine (DZ) is poorly

soluble in water with a short half-life in blood circulation, low rate of response with the toxic effect which ultimately limits its utilization of the treatment of skin cancer⁷⁰. IC₅₀ of DZNP was 0.19 mg/mL, while the IC₅₀ was 0.63 mg/ml for DZNC, with higher values than the ones obtained for our nanosystems. Besides, it is possible to compare the Te nanostructures synthesized in this work with commercially available anticancer treatments in terms of cost. For instance, dacarbazine intravenous nanopowder has a price for injection (100 mg) of around USD \$88/supply, while the price of 100 mg of Na₂TeO₃, the precursor of the Te nanoparticles, is around 1\$ (plus the price of orange, lemon and lime, that rounds between 0.5-0.9 USD \$/kg)⁷¹. Therefore, it is possible to conclude that the Te nanosystems presented in this work are relatively more efficient and cost-effective than other current nanoparticle-based treatments towards melanoma.

ROS production was compared with an inorganic nanoparticle, Iron Sucrose (IS) (Venofer®, American Regent, Shirley, NY). Gupta et al. found that incubation with 100 µg/mL IS induced significantly higher ROS generation compared to control. IS appeared to increase intracellular ROS in a time-dependent manner and a 60% increase from control experiments was measured after incubation with IS⁷². For all our nanoparticles systems, after 24 hours of incubation, there was around 20-30% increase from control experiments.

Cell fixation and SEM imaging

The effect of the different Te nanoparticles in the morphology and proliferation of both HDF and melanoma cells were extensively studied using SEM microscopy (Figure 11). When HDF cells were cultured in presence of a fixed concentration of OR- (Figure 11B), LEM- (Figure 11C) and

LIM-TeNP (Figure 11D) showed no significant modification on the cell morphology in contrast with the control (Figure 11A). Therefore, these results suggest that the proliferation of the cells is maintained constant when they are grown in presence of the Te nanoparticles. Nonetheless, it can be observed some discontinuities on the membrane previous to rupture (without any other change in the structure), which eventually end on cell death. Hence, the tendency of these results suggested a necrosis mechanism^{73,74}.

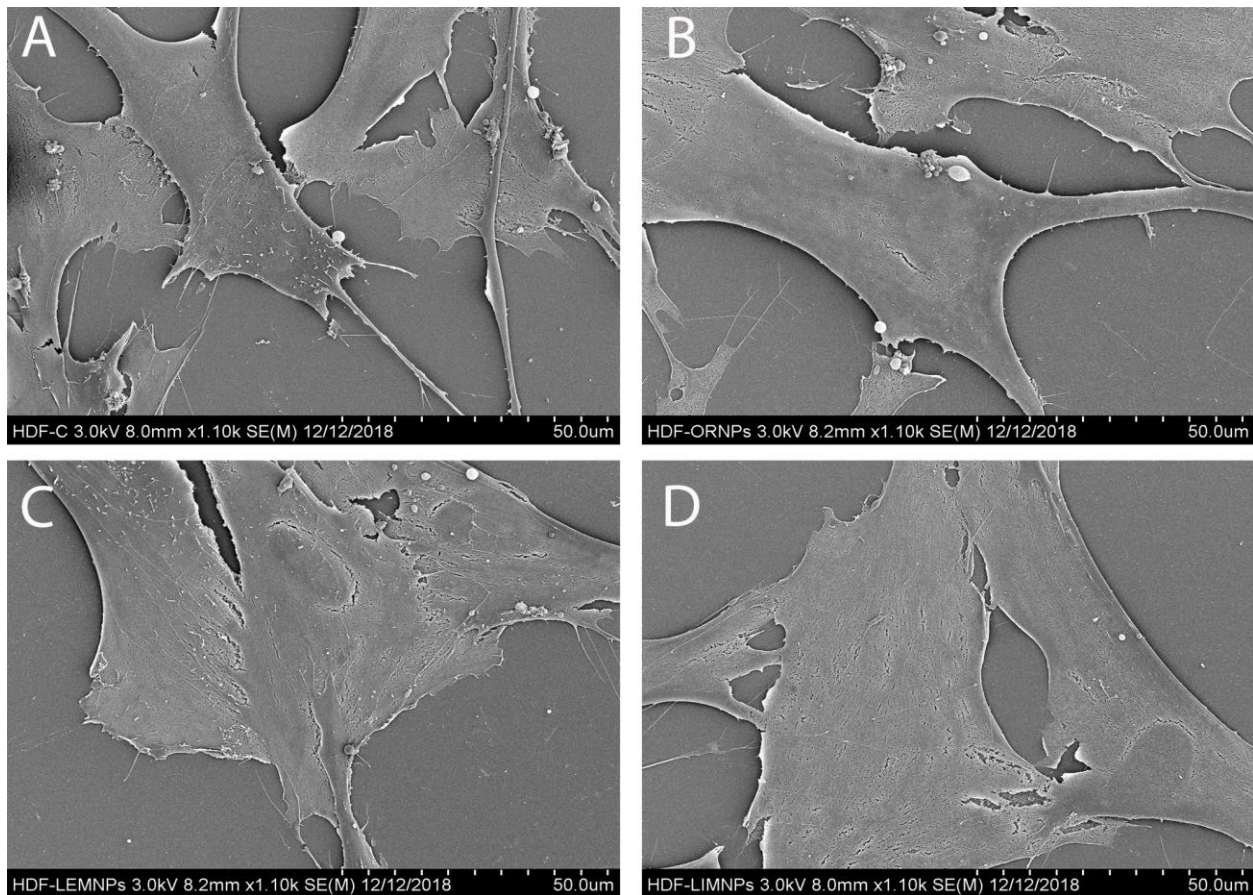


Figure 11. SEM images showing the interaction between HDF cells and OR- (B), LEM- (C) and LIM-TeNPs (D). Interaction with 0 µg/mL (A) and 50 µg/mL (B, C, D) of the respective Te nanoparticles and HDF cells were analyzed.

On the contrary, when melanoma cells were cultured in presence of a fixed concentration of OR- (Figure 12B), LEM- (Figure 12C) and LIM-TeNPs (Figure 12D) significant morphological changes were observed in respect with the control (Figure 12A). In all cases, the cell membrane suffered significant damages and showed different stages on cell death mechanism. Swelling on the membrane appeared due to the rearranging of the structures in the cytoskeleton (Figure 12C) as a consequence of the apoptosis mechanism induced by the cells⁷⁵. Finally, these formations produce cell membrane rupture in various fragments (Figures 12B and 12D) that end in cell death⁷⁶. Therefore, a significant decay in cell proliferation can be found, with important differences between the treated and untreated samples.

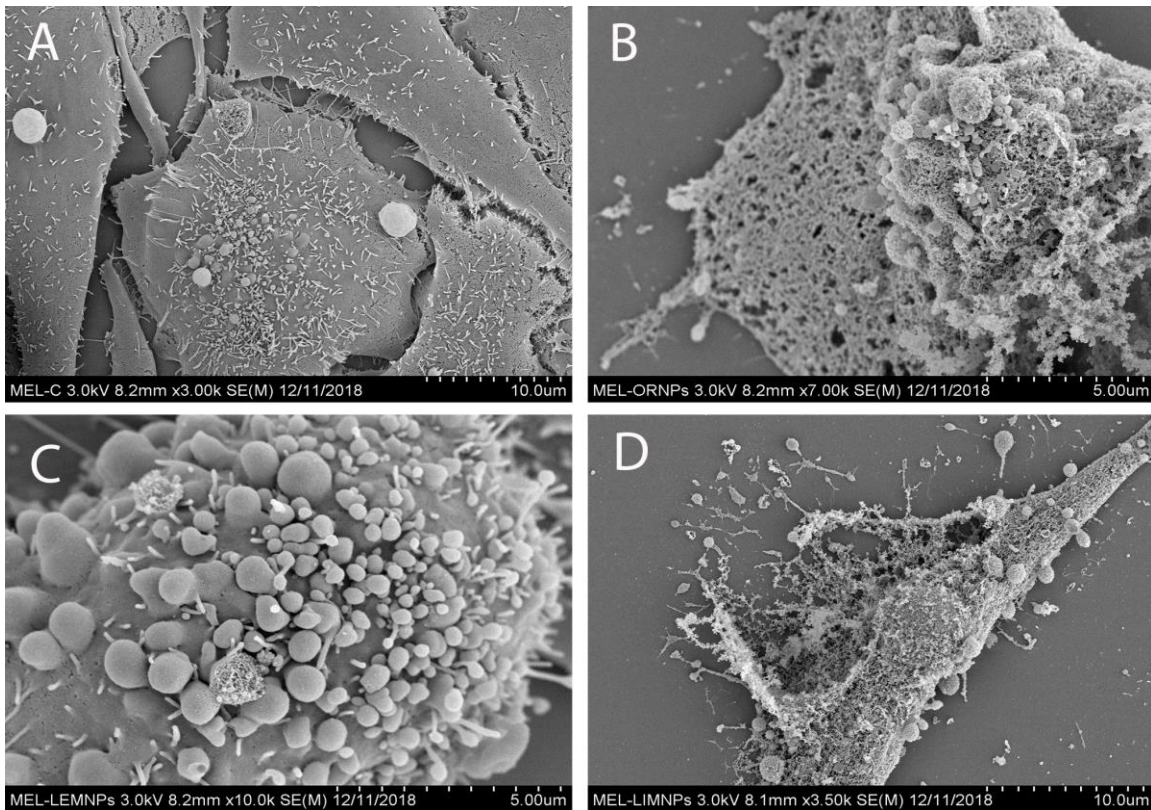


Figure 12. SEM images showing the interaction between melanoma cells and OR- (B), LEM- (C) and LIM-TeNPs (D). Interaction with 0 $\mu\text{g/mL}$ (A) and 50 $\mu\text{g/mL}$ (B, C, D) of the respective Te nanoparticles and melanoma cells were analyzed.

Conclusions

In this work, an effective green and environmentally-friendly synthesis route for TeNPs synthesis was presented, employing three citric juices (orange, lemon and lime) as unique reducing and stabilizing agents in a reaction that was accomplished in seconds. TeNPs, with either rod-like or cubic-shaped morphologies were extensively characterized in terms of composition and chemical structure, before being employed as biomedical agents. Inhibition of antibiotic-resistant bacterial growth was found in a range of concentrations between 5 and 50 $\mu\text{g/mL}$ with a main mechanism of inhibition related to ROS production. Cytotoxicity studies were accomplished showing a dose-dependent anticancer effect towards human melanoma cells in a range of concentrations up to 100 $\mu\text{g/mL}$, remaining cytocompatible towards human healthy fibroblast cells at concentrations up to 50 $\mu\text{g/mL}$. Therefore, citric juices-mediated TeNPs are shown as a novel nanosized agent with antimicrobial and anticancer properties, enhanced cytocompatibility, with an easy synthesis that does not imply the use of harsh materials or the production of toxic by-products. These findings suggest that green-synthesized TeNPs can overcome many of the shortcomings of traditionally synthesized nanomaterials, providing a promising evidence for future research and applications in medicine of this rare metalloid in its nanometer scale, for instance, in antibacterial wound dressings.

Acknowledgements

This work was supported by the Chemical Engineering Department at Northeastern University. Funding from MINECO (MAT2014-59772-C2-1-P and MAT2014-59772-C2-2-P) and European Union [grant number ERC-2013-SyG 610256 NANOCOSMOS] is acknowledged. We also acknowledge the service from the MiNa Laboratory at IMN funded by CM (S2013/ICE2822), MINECO (CSIC13-4E-1794) and the EU (FEDER, FSE). JLCD thanks the School of Engineering and Sciences at Tecnológico de Monterrey through the Research Group on Photonics and Quantum Systems for financial support.

Supplementary information

Figures

- **Figure S1.** Coloration of reaction mixture after microwave-assisted synthetic approaches for different concentrations.
- **Figure S2.** TEM characterization of OR-TeNPs when 100 mM (A), 75 mM (B), 50 mM (C) and 25 mM (D) metallic salt precursor concentration was used.
- **Figure S3.** TEM characterization of LEM-TeNPs when 100 mM (A), 75 mM (B), 50 mM (C) and 25 mM (D) metallic salt precursor concentration was used.
- **Figure S4.** TEM characterization of LIM-TeNPs when 100 mM (A), 75 mM (B), 50 mM (C) and 25 mM (D) metallic salt precursor concentration was used.
- **Figure S5.** EDX characterization of OR-TeNPs.
- **Figure S6.** EDX characterization of LEM-TeNPs.
- **Figure S7.** EDX characterization of LIM-TeNPs.
- **Figure S8.** XPS Core level spectra of Te 3d (left), C 1s (center) and O 1s (right) of OR-, LEM- and LIM-TeNPs, respectively.

- **Figure S9.** TEM images of OR- (A), LEM- (B) and LIM- (C) TeNPs after 60 days of synthesis.
- **Figure S10.** Citric-mediated TeNPs decrease the growth of Escherichia coli (A, C, E) and Staphylococcus aureus (B, D, F).
- **Figure S11.** Gompertz parameters evaluation.

Tables

- **Table S1.** Lattice parameters calculated for Orange-TeNPs (h-Te) and, Lemon-TeNPs and Lime-TeNPs (β -TeO₂).
- **Table S2.** Composition of the samples extracted from the wide energy range scans displayed in Figure S8.
- **Table S3.** Components used for the fitting of the C 1s and O 1s core levels.
- **Table S4.** Zeta-potential values for freshly and 60-days old OR-, LEM- and LIM-TeNPs.

References

- (1) Ventola, C. L. The Antibiotic Resistance Crisis: Part 1: Causes and Threats. *P T* **2015**, *40* (4), 277–283.
- (2) Zaman, S. Bin; Hussain, M. A.; Nye, R.; Mehta, V.; Mamun, K. T.; Hossain, N. A Review on Antibiotic Resistance: Alarm Bells Are Ringing. *Cureus* **2017**, *9* (6), e1403. <https://doi.org/10.7759/cureus.1403>.
- (3) Li, B.; Webster, T. J. Bacteria Antibiotic Resistance: New Challenges and Opportunities for Implant-Associated Orthopedic Infections. *J. Orthop. Res.* **2017**, *36* (1), 22–32. <https://doi.org/10.1002/jor.23656>.
- (4) Housman, G.; Byler, S.; Heerboth, S.; Lapinska, K.; Longacre, M.; Snyder, N.; Sarkar, S. Drug Resistance in Cancer: An Overview. *Cancers (Basel)*. **2014**, *6* (3), 1769–1792. <https://doi.org/10.3390/cancers6031769>.
- (5) Siegel, R. L.; Miller, K. D.; Jemal, A. Cancer Statistics, 2018. *CA. Cancer J. Clin.* **2018**, *68* (1), 7–30. <https://doi.org/10.3322/caac.21442>.
- (6) Kulkarni, R. P. Nano-Bio-Genesis: Tracing the Rise of Nanotechnology and Nanobiotechnology as “Big Science”. *J. Biomed. Discov. Collab.* **2007**, *2*, 3. <https://doi.org/10.1186/1747-5333-2-3>.
- (7) Ventola, C. L. The Nanomedicine Revolution: Part 1: Emerging Concepts. *P T* **2012**, *37* (9), 512–525.
- (8) Rizzo, L. Y.; Theek, B.; Storm, G.; Kiessling, F.; Lammers, T. Recent Progress in Nanomedicine: Therapeutic, Diagnostic and Theranostic Applications. *Curr. Opin. Biotechnol.* **2013**, *24* (6), 1159–1166. <https://doi.org/10.1016/j.copbio.2013.02.020>.
- (9) Murthy, S. K. Nanoparticles in Modern Medicine: State of the Art and Future Challenges.

- Int. J. Nanomedicine* **2007**, 2 (2), 129–141.
- (10) Salata, O. Applications of Nanoparticles in Biology and Medicine. *J. Nanobiotechnology* **2004**, 2 (1), 3. <https://doi.org/10.1186/1477-3155-2-3>.
- (11) Escárcega-González, C. E.; Garza-Cervantes, J. A.; Vazquez-Rodríguez, A.; Montelongo-Peralta, L. Z.; Treviño-Gonzalez, M. T.; Díaz Barriga Castro, E.; Saucedo-Salazar, E. M.; Chávez Morales, R. M.; Regalado-Soto, D. I.; Treviño-González, F. M.; et al. In Vivo Antimicrobial Activity of Silver Nanoparticles Produced via a Green Chemistry Synthesis Using *Acacia Rigidula* as a Reducing and Capping Agent. *Int. J. Nanomedicine* **2018**, Volume 13, 2349–2363. <https://doi.org/10.2147/IJN.S160605>.
- (12) Arvizo, R.; Bhattacharya, R.; Mukherjee, P. Gold Nanoparticles: Opportunities and Challenges in Nanomedicine. *Expert Opin. Drug Deliv.* **2010**, 7 (6), 753–763. <https://doi.org/10.1517/17425241003777010>.
- (13) Bogdan, J.; Pławińska-Czarnak, J.; Zarzyńska, J. Nanoparticles of Titanium and Zinc Oxides as Novel Agents in Tumor Treatment: A Review. *Nanoscale Res. Lett.* **2017**, 12 (1), 225. <https://doi.org/10.1186/s11671-017-2007-y>.
- (14) Jiang, J.; Pi, J.; Cai, J. The Advancing of Zinc Oxide Nanoparticles for Biomedical Applications. *Bioinorg. Chem. Appl.* **2018**, 2018, 1–18. <https://doi.org/10.1155/2018/1062562>.
- (15) Tang, L.; Cheng, J. Nonporous Silica Nanoparticles for Nanomedicine Application. *Nano Today* **2013**, 8 (3), 290–312. <https://doi.org/10.1016/J.NANTOD.2013.04.007>.
- (16) Yamashita, T.; Yamashita, K.; Nabeshi, H.; Yoshikawa, T.; Yoshioka, Y.; Tsunoda, S.-I.; Tsutsumi, Y. Carbon Nanomaterials: Efficacy and Safety for Nanomedicine. *Mater. (Basel, Switzerland)* **2012**, 5 (2), 350–363. <https://doi.org/10.3390/ma5020350>.

- (17) Zhao, Y.; Sun, Q.; Zhang, X.; Baeyens, J.; Su, H. Self-Assembled Selenium Nanoparticles and Their Application in the Rapid Diagnostic Detection of Small Cell Lung Cancer Biomarkers. *Soft Matter* **2018**, *14* (4), 481–489. <https://doi.org/10.1039/c7sm01687e>.
- (18) Hosnedlova, B.; Kepinska, M.; Skalickova, S.; Fernandez, C.; Ruttkay-Nedecky, B.; Peng, Q.; Baron, M.; Melcova, M.; Opatrilova, R.; Zidkova, J.; et al. Nano-Selenium and Its Nanomedicine Applications: A Critical Review. *Int. J. Nanomedicine* **2018**, *Volume 13*, 2107–2128. <https://doi.org/10.2147/IJN.S157541>.
- (19) Zonaro, E.; Lampis, S.; Turner, R. J.; Qazi, S. J. S.; Vallini, G. Biogenic Selenium and Tellurium Nanoparticles Synthesized by Environmental Microbial Isolates Efficaciously Inhibit Bacterial Planktonic Cultures and Biofilms. *Front. Microbiol.* **2015**, *6*, 584. <https://doi.org/10.3389/fmicb.2015.00584>.
- (20) Fleming, A. On the Specific Antibacterial Properties of Penicillin and Potassium Tellurite. Incorporating a Method of Demonstrating Some Bacterial Antagonisms. *J. Pathol. Bacteriol.* **1932**, *35* (6), 831–842. <https://doi.org/10.1002/path.1700350603>.
- (21) Ramos-Ruiz, A.; Wilkening, J. V.; Field, J. A.; Sierra-Alvarez, R. Leaching of Cadmium and Tellurium from Cadmium Telluride (CdTe) Thin-Film Solar Panels under Simulated Landfill Conditions. *J. Hazard. Mater.* **2017**, *336*, 57–64. <https://doi.org/10.1016/j.jhazmat.2017.04.052>.
- (22) Poplawsky, J. D.; Guo, W.; Paudel, N.; Ng, A.; More, K.; Leonard, D.; Yan, Y. Structural and Compositional Dependence of the CdTe_xSe_{1-x} Alloy Layer Photoactivity in CdTe-Based Solar Cells. *Nat. Commun.* **2016**, *7* (1), 12537. <https://doi.org/10.1038/ncomms12537>.
- (23) Molina-Quiroz, R. C.; Muñoz-Villagrán, C. M.; de la Torre, E.; Tantaleán, J. C.; Vásquez,

- C. C.; Pérez-Donoso, J. M. Enhancing the Antibiotic Antibacterial Effect by Sub Lethal Tellurite Concentrations: Tellurite and Cefotaxime Act Synergistically in Escherichia Coli. *PLoS One* **2012**, 7 (4), e35452. <https://doi.org/10.1371/journal.pone.0035452>.
- (24) Pérez, J. M.; Calderón, I. L.; Arenas, F. A.; Fuentes, D. E.; Pradenas, G. A.; Fuentes, E. L.; Sandoval, J. M.; Castro, M. E.; Elías, A. O.; Vásquez, C. C. Bacterial Toxicity of Potassium Tellurite: Unveiling an Ancient Enigma. *PLoS One* **2007**, 2 (2), e211. <https://doi.org/10.1371/journal.pone.0000211>.
- (25) Liu, J.; Liang, C.; Zhu, X.; Lin, Y.; Zhang, H.; Wu, S. Understanding the Solvent Molecules Induced Spontaneous Growth of Uncapped Tellurium Nanoparticles. *Sci. Rep.* **2016**, 6, 32631. <https://doi.org/10.1038/srep32631>.
- (26) Ray, P. C.; Yu, H.; Fu, P. P. Toxicity and Environmental Risks of Nanomaterials: Challenges and Future Needs. *J. Environ. Sci. Health. C. Environ. Carcinog. Ecotoxicol. Rev.* **2009**, 27 (1), 1–35. <https://doi.org/10.1080/10590500802708267>.
- (27) Mukherjee, S.; Patra, C. R. Biologically Synthesized Metal Nanoparticles: Recent Advancement and Future Perspectives in Cancer Theranostics. *Futur. Sci. OA* **2017**, 3 (3), FSO203. <https://doi.org/10.4155/fsoa-2017-0035>.
- (28) Salamanca-Buentello, F.; Persad, D. L.; Court, E. B.; Martin, D. K.; Daar, A. S.; Singer, P. A. Nanotechnology and the Developing World. *PLoS Med.* **2005**, 2 (5), e97. <https://doi.org/10.1371/journal.pmed.0020097>.
- (29) Iavicoli, I.; Leso, V.; Ricciardi, W.; Hodson, L. L.; Hoover, M. D. Opportunities and Challenges of Nanotechnology in the Green Economy. *Environ. Heal.* **2014**, 13 (1), 78. <https://doi.org/10.1186/1476-069X-13-78>.
- (30) de la Guardia, M. The Challenges of Green Nanotechnology. *Bioimpacts* **2014**, 4 (1), 1–2.

<https://doi.org/10.5681/bi.2014.009>.

- (31) Makarov, V. V.; Love, A. J.; Sinitsyna, O. V.; Makarova, S. S.; Yaminsky, I. V.; Taliansky, M. E.; Kalinina, N. O. "Green" Nanotechnologies: Synthesis of Metal Nanoparticles Using Plants. *Acta Naturae* **2014**, 6 (1), 35–44.
- (32) Kim, Y.-J.; Mathiyalagan, R.; Markus, J.; Wang, C.; Singh, P.; Ahn, S.; Farh, M. E.-A.; Yang, D. C.; Abbai, R. Green Synthesis of Multifunctional Silver and Gold Nanoparticles from the Oriental Herbal Adaptogen: Siberian Ginseng. *Int. J. Nanomedicine* **2016**, Volume 11, 3131–3143. <https://doi.org/10.2147/IJN.S108549>.
- (33) Medina Cruz, D.; Mi, G.; Webster, T. J. Synthesis and Characterization of Biogenic Selenium Nanoparticles with Antimicrobial Properties Made by *Staphylococcus Aureus* , Methicillin-Resistant *Staphylococcus Aureus* (MRSA), *Escherichia Coli*, and *Pseudomonas Aeruginosa*. *J. Biomed. Mater. Res. Part A* **2018**, 106 (5), 1400–1412. <https://doi.org/10.1002/jbm.a.36347>.
- (34) Niknejad, F.; Nabili, M.; Daie Ghazvini, R.; Moazeni, M. Green Synthesis of Silver Nanoparticles: Another Honor for the Yeast Model *Saccharomyces Cerevisiae*. *Curr. Med. Mycol.* **2015**, 1 (3), 17–24. <https://doi.org/10.18869/acadpub.cmm.1.3.17>.
- (35) Velusamy, P.; Kumar, G. V.; Jeyanthi, V.; Das, J.; Pachaiappan, R. Bio-Inspired Green Nanoparticles: Synthesis, Mechanism, and Antibacterial Application. *Toxicol. Res.* **2016**, 32 (2), 95–102. <https://doi.org/10.5487/TR.2016.32.2.095>.
- (36) Wu, L.; Cai, X.; Nelson, K.; Xing, W.; Xia, J.; Zhang, R.; Stacy, A. J.; Luderer, M.; Lanza, G. M.; Wang, L. V.; et al. A Green Synthesis of Carbon Nanoparticles from Honey and Their Use in Real-Time Photoacoustic Imaging. *Nano Res.* **2013**, 6 (5), 312–325. <https://doi.org/10.1007/s12274-013-0308-8>.

- (37) Nune, S. K.; Chanda, N.; Shukla, R.; Katti, K.; Kulkarni, R. R.; Thilakavathi, S.; Mekapothula, S.; Kannan, R.; Katti, K. V. Green Nanotechnology from Tea: Phytochemicals in Tea as Building Blocks for Production of Biocompatible Gold Nanoparticles. *J. Mater. Chem.* **2009**, *19* (19), 2912–2920.
<https://doi.org/10.1039/b822015h>.
- (38) Singh, P.; Pandit, S.; Garnæs, J.; Tunjic, S.; Mokkalpati, V.; Sultan, A.; Thygesen, A.; Mackevica, A.; Mateiu, R. V.; Daugaard, A. E.; et al. Green Synthesis of Gold and Silver Nanoparticles from *Cannabis Sativa* (Industrial Hemp) and Their Capacity for Biofilm Inhibition. *Int. J. Nanomedicine* **2018**, *Volume 13*, 3571–3591.
<https://doi.org/10.2147/IJN.S157958>.
- (39) Lee, J. H.; Moon, M. C.; Lee, J. Y.; Yu, I. J. Challenges and Perspectives of Nanoparticle Exposure Assessment. *Toxicol. Res.* **2010**, *26* (2), 95–100.
<https://doi.org/10.5487/TR.2010.26.2.095>.
- (40) Kong, B.; Seog, J. H.; Graham, L. M.; Lee, S. B. Experimental Considerations on the Cytotoxicity of Nanoparticles. *Nanomedicine* **2011**, *6* (5), 929–941.
<https://doi.org/10.2217/nnm.11.77>.
- (41) Kelebek, H.; Selli, S.; Canbas, A.; Cabaroglu, T. HPLC Determination of Organic Acids, Sugars, Phenolic Compositions and Antioxidant Capacity of Orange Juice and Orange Wine Made from a Turkish Cv. Kozan. *Microchem. J.* **2009**, *91* (2), 187–192.
<https://doi.org/10.1016/J.MICROC.2008.10.008>.
- (42) Penniston, K. L.; Nakada, S. Y.; Holmes, R. P.; Assimos, D. G. Quantitative Assessment of Citric Acid in Lemon Juice, Lime Juice, and Commercially-Available Fruit Juice Products. *J. Endourol.* **2008**, *22* (3), 567–570. <https://doi.org/10.1089/end.2007.0304>.

- (43) Bennett, A. H.; Tarbert, D. J. Vitamin C in Citrus Juices. *Biochem. J.* **1933**, *27* (4), 1294–1301.
- (44) Briggs, D. Handbook of X-Ray Photoelectron Spectroscopy C. D. Wanger, W. M. Riggs, L. E. Davis, J. F. Moulder and G. E. Muilenberg Perkin-Elmer Corp., Physical Electronics Division, Eden Prairie, Minnesota, USA, 1979. 190 Pp. \$195. *Surf. Interface Anal.* **1981**, *3* (4), v–v. <https://doi.org/10.1002/sia.740030412>.
- (45) Silva, R. R.; Mejia, H. A. G.; Ribeiro, S. J. L.; Shrestha, L. K.; Ariga, K.; Oliveira Jr., O. N.; Camargo, V. R.; Maia, L. J. Q.; Araújo, C. B.; Silva, R. R.; et al. Facile Synthesis of Tellurium Nanowires and Study of Their Third-Order Nonlinear Optical Properties. *J. Braz. Chem. Soc.* **2016**, *28* (1), 58–67. <https://doi.org/10.5935/0103-5053.20160145>.
- (46) Zwietering, M. H.; Jongenburger, I.; Rombouts, F. M.; van 't Riet, K. Modeling of the Bacterial Growth Curve. *Appl. Environ. Microbiol.* **1990**, *56* (6), 1875–1881.
- (47) Kim, H.; Seo, Y. S.; Kim, K.; Han, J. W.; Park, Y.; Cho, S. Concentration Effect of Reducing Agents on Green Synthesis of Gold Nanoparticles: Size, Morphology, and Growth Mechanism. *Nanoscale Res. Lett.* **2016**, *11* (1), 230. <https://doi.org/10.1186/s11671-016-1393-x>.
- (48) Adenis, C.; Langer, V.; Lindqvist, O. Reinvestigation of the Structure of Tellurium. *Acta Crystallogr. Sect. C Cryst. Struct. Commun.* **1989**, *45* (6), 941–942. <https://doi.org/10.1107/S0108270188014453>.
- (49) Beyer, H. Verfeinerung Der Kristallstruktur von Tellurit, Dem Rhomischen TeO₂. *Zeitschrift fur Krist.* **1967**, *124*, 228–237.
- (50) Kondratyuk, I. P.; Muradyan, L. A.; Pisarevskii, Y. V.; Simonov, V. I. Precision X-Ray Structural Investigation of Acousto-Optical Single Crystals of α -TeO₂. *Kristallografiya*

- 1987**, 32, 609.
- (51) Kefford, J. F. The Chemical Constituents of Citrus Fruits. *Adv. Food Res.* **1960**, 9, 285–372. [https://doi.org/10.1016/S0065-2628\(08\)60278-5](https://doi.org/10.1016/S0065-2628(08)60278-5).
- (52) SCOTT, W. C.; KEW, T. J.; VELDHUIS, M. K. Composition of Orange Juice Cloud. *J. Food Sci.* **1965**, 30 (5), 833–837. <https://doi.org/10.1111/j.1365-2621.1965.tb01850.x>.
- (53) Vandercook, C. E.; Stephenson, R. G. Lemon Juice Composition. Identification of Major Phenolic Compounds and Estimation by Paper Chromatography. *J. Agric. Food Chem.* **1966**, 14 (5), 450–454. <https://doi.org/10.1021/jf60147a003>.
- (54) VANDERCOOK, C. E.; ROLLE, L. A.; POSTLMAYR, H. L.; UTTERBERG, R. A. Lemon Juice Composition. V. Effects of Some Fruit Storage and Processing Variables on the Characterization of Lemon Juice. *J. Food Sci.* **1966**, 31 (1), 58–62. <https://doi.org/10.1111/j.1365-2621.1966.tb15415.x>.
- (55) Berezin, K. V.; Shagautdinova, I. T.; Chernavina, M. L.; Novoselova, A. V.; Dvoretiskii, K. N.; Likhter, A. M. The Experimental Vibrational Infrared Spectrum of Lemon Peel and Simulation of Spectral Properties of the Plant Cell Wall. *Opt. Spectrosc.* **2017**, 123 (3), 495–500. <https://doi.org/10.1134/S0030400X17090089>.
- (56) Carotenuto, G.; Palomba, M.; De Nicola, S.; Ambrosone, G.; Coscia, U. Structural and Photoconductivity Properties of Tellurium/PMMA Films. *Nanoscale Res. Lett.* **2015**, 10 (1), 313. <https://doi.org/10.1186/s11671-015-1007-z>.
- (57) El-Mallawany, R. A. Theoretical and Experimental IR Spectra of Binary Rare Earth Tellurite Glasses—1. *Infrared Phys.* **1989**, 29 (2–4), 781–785. [https://doi.org/10.1016/0020-0891\(89\)90125-5](https://doi.org/10.1016/0020-0891(89)90125-5).
- (58) Zare, B.; Faramarzi, M. A.; Sepehrizadeh, Z.; Shakibaie, M.; Rezaie, S.; Shahverdi, A. R.

- Biosynthesis and Recovery of Rod-Shaped Tellurium Nanoparticles and Their Bactericidal Activities. *Mater. Res. Bull.* **2012**, 47 (11), 3719–3725.
<https://doi.org/10.1016/J.MATERRESBULL.2012.06.034>.
- (59) Pal, S.; Tak, Y. K.; Song, J. M. Does the Antibacterial Activity of Silver Nanoparticles Depend on the Shape of the Nanoparticle? A Study of the Gram-Negative Bacterium *Escherichia Coli*. *Appl. Environ. Microbiol.* **2007**, 73 (6), 1712–1720.
<https://doi.org/10.1128/AEM.02218-06>.
- (60) Zannoni, D.; Borsetti, F.; Harrison, J. J.; Turner, R. J. The Bacterial Response to the Chalcogen Metalloids Se and Te. In *Advances in microbial physiology*; 2007; Vol. 53, pp 1–312. [https://doi.org/10.1016/S0065-2911\(07\)53001-8](https://doi.org/10.1016/S0065-2911(07)53001-8).
- (61) Pi, J.; Yang, F.; Jin, H.; Huang, X.; Liu, R.; Yang, P.; Cai, J. Selenium Nanoparticles Induced Membrane Bio-Mechanical Property Changes in MCF-7 Cells by Disturbing Membrane Molecules and F-Actin. *Bioorg. Med. Chem. Lett.* **2013**, 23 (23), 6296–6303.
<https://doi.org/10.1016/j.bmcl.2013.09.078>.
- (62) Benedec, D.; Oniga, I.; Cuibus, F.; Sevastre, B.; Stiufiuc, G.; Duma, M.; Hanganu, D.; Iacovita, C.; Stiufiuc, R.; Lucaciu, C. M. *Origanum Vulgare* Mediated Green Synthesis of Biocompatible Gold Nanoparticles Simultaneously Possessing Plasmonic, Antioxidant and Antimicrobial Properties. *Int. J. Nanomedicine* **2018**, Volume 13, 1041–1058. <https://doi.org/10.2147/IJN.S149819>.
- (63) Gurunathan, S.; Han, J.; Park, J. H.; Kim, J.-H. A Green Chemistry Approach for Synthesizing Biocompatible Gold Nanoparticles. *Nanoscale Res. Lett.* **2014**, 9 (1), 248.
<https://doi.org/10.1186/1556-276X-9-248>.
- (64) Ba, L. A.; Döring, M.; Jamier, V.; Jacob, C. Tellurium: An Element with Great Biological

- Potency and Potential. *Org. Biomol. Chem.* **2010**, 8 (19), 4203–4216.
<https://doi.org/10.1039/c0Ob00086h>.
- (65) Brown, C. D.; Cruz, D. M.; Roy, A. K.; Webster, T. J. Synthesis and Characterization of PVP-Coated Tellurium Nanorods and Their Antibacterial and Anticancer Properties. *J. Nanoparticle Res.* **2018**, 20 (9), 254. <https://doi.org/10.1007/s11051-018-4354-8>.
- (66) Chen, X.; Lv, Q.; Liu, Y.; Deng, W. Effect of Food Additive Citric Acid on The Growth of Human Esophageal Carcinoma Cell Line EC109. *Cell J.* **2017**, 18 (4), 493–502.
<https://doi.org/10.22074/CELLJ.2016.4716>.
- (67) van der Reest, J.; Gottlieb, E. Anti-Cancer Effects of Vitamin C Revisited. *Cell Res.* **2016**, 26 (3), 269–270. <https://doi.org/10.1038/cr.2016.7>.
- (68) Brenneisen, P.; Reichert, A. Nanotherapy and Reactive Oxygen Species (ROS) in Cancer: A Novel Perspective. *Antioxidants* **2018**, 7 (2), 31. <https://doi.org/10.3390/antiox7020031>.
- (69) Hafeez, A.; Kazmi, I. Dacarbazine Nanoparticle Topical Delivery System for the Treatment of Melanoma. *Sci. Rep.* **2017**, 7 (1), 16517. <https://doi.org/10.1038/s41598-017-16878-1>.
- (70) Dacarbazine Prices, Coupons & Patient Assistance Programs - Drugs.com
<https://www.drugs.com/price-guide/dacarbazine> (accessed Dec 24, 2018).
- (71) United States Department of Agriculture National Agricultural Statistics Service.
- (72) Gupta, A.; Zhuo, J.; Zha, J.; Reddy, S.; Olp, J.; Pai, A. Effect of Different Intravenous Iron Preparations on Lymphocyte Intracellular Reactive Oxygen Species Generation and Subpopulation Survival. *BMC Nephrol.* **2010**, 11, 16. <https://doi.org/10.1186/1471-2369-11-16>.
- (73) Sun, H.; Jia, J.; Jiang, C.; Zhai, S. Gold Nanoparticle-Induced Cell Death and Potential

Applications in Nanomedicine. *Int. J. Mol. Sci.* **2018**, *19* (3), 754.

<https://doi.org/10.3390/ijms19030754>.

- (74) Burattini, S.; Falcieri, E. Analysis of Cell Death by Electron Microscopy. In *Methods in molecular biology (Clifton, N.J.)*; 2013; Vol. 1004, pp 77–89. https://doi.org/10.1007/978-1-62703-383-1_7.
- (75) Taatjes, D. J.; Sobel, B. E.; Budd, R. C. Morphological and Cytochemical Determination of Cell Death by Apoptosis. *Histochem. Cell Biol.* **2008**, *129* (1), 33–43. <https://doi.org/10.1007/s00418-007-0356-9>.
- (76) Elmore, S. Apoptosis: A Review of Programmed Cell Death. *Toxicol. Pathol.* **2007**, *35* (4), 495–516. <https://doi.org/10.1080/01926230701320337>.

Supplementary information

Citric juice-mediated Synthesis of Tellurium Nanoparticles with Antimicrobial and Anticancer Properties

David Medina^{1,†}, William Tien-Street^{1,2,†}, Bohan Zhang^{1,†}, Xinjing Huang^{1,†}, Ada Vernet Crua¹, Alfonso Nieto-Argüello³, Jorge L. Cholula-Díaz³, Lidia Martínez⁴, Yves Huttel⁴, María Ujué González⁵, José Miguel García-Martín⁵ and Thomas J. Webster^{1,*}

†These authors contributed equally to this paper.

¹ Department of Chemical Engineering, Northeastern University, Boston, MA 02115, USA

² Department of Bioengineering, Northeastern University, Boston, MA 02115, USA

³ School of Engineering and Sciences, Tecnológico de Monterrey, Av. Eugenio Garza Sada 2501, Monterrey, NL 64849, Mexico.

⁴ Materials Science Factory. Instituto de Ciencia de Materiales de Madrid, ICMM-CSIC, Sor Juana Inés de la Cruz 3, 28049 Madrid, Spain

⁵ Instituto de Micro y Nanotecnología, IMN-CNM, CSIC (CEI UAM+CSIC), Isaac Newton 8, 28760 Tres Cantos, Spain

*Correspondence: Thomas J. Webster

Department of Chemical Engineering, Northeastern University,

313 Snell Engineering Center, 360 Huntington Avenue, Boston, MA 02115

Tel +1 617 373 6585

Fax +1 617 373 2209; Email: th.webster@neu.edu

Synthesis of TeNPs

Color change within the solution after microwave-assisted reaction at different metallic salts concentrations for LEM-TeNPs employing lemon juice extract (Figure S1). Identical results were found when the other extracts –orange and lime- were employed. The coloration appeared a few seconds after the heating cycle.

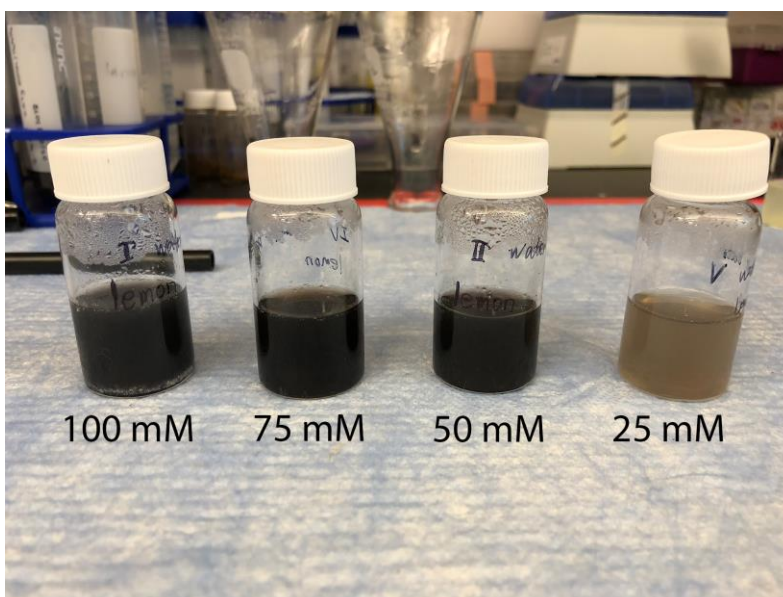


Figure S1. Coloration of reaction mixture after microwave-assisted synthetic approaches for different Te-precursor solution concentrations. From left to right, a decrease of the metallic salt (sodium tellurite) concentration is translated in a brighten of the black coloration within the solution.

TEM characterization of TeNPs

OR-, LEM- and LIM-TeNPs were prepared using a microwave-assisted method with a decrease of the Te-precursor solution concentration from 100 to 25 mM, leading to some changes in the morphology and aggregation of the structures, with the presence of clusters at high concentrations (Figures S2, S3 and S4).

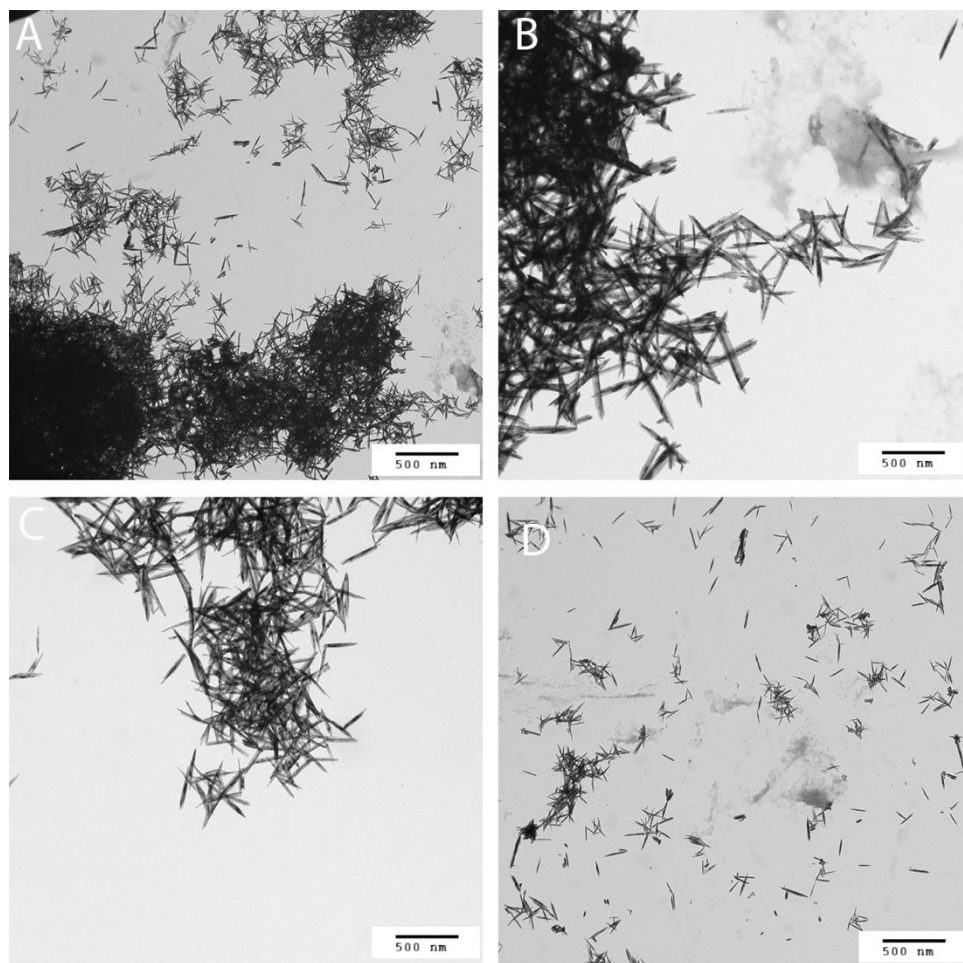


Figure S2. TEM characterization of OR-TeNPs when 100 mM (A), 75 mM (B), 50 mM (C) and 25 mM (D) Te-precursor solution concentration was used.

For OR-TeNPs, needle-like nanostructures were found to generate clusters at high concentrations, with less presence of the aggregates when the concentration of Te-precursor solution was decreased, while the morphology was the same for all the samples (Figure S2).

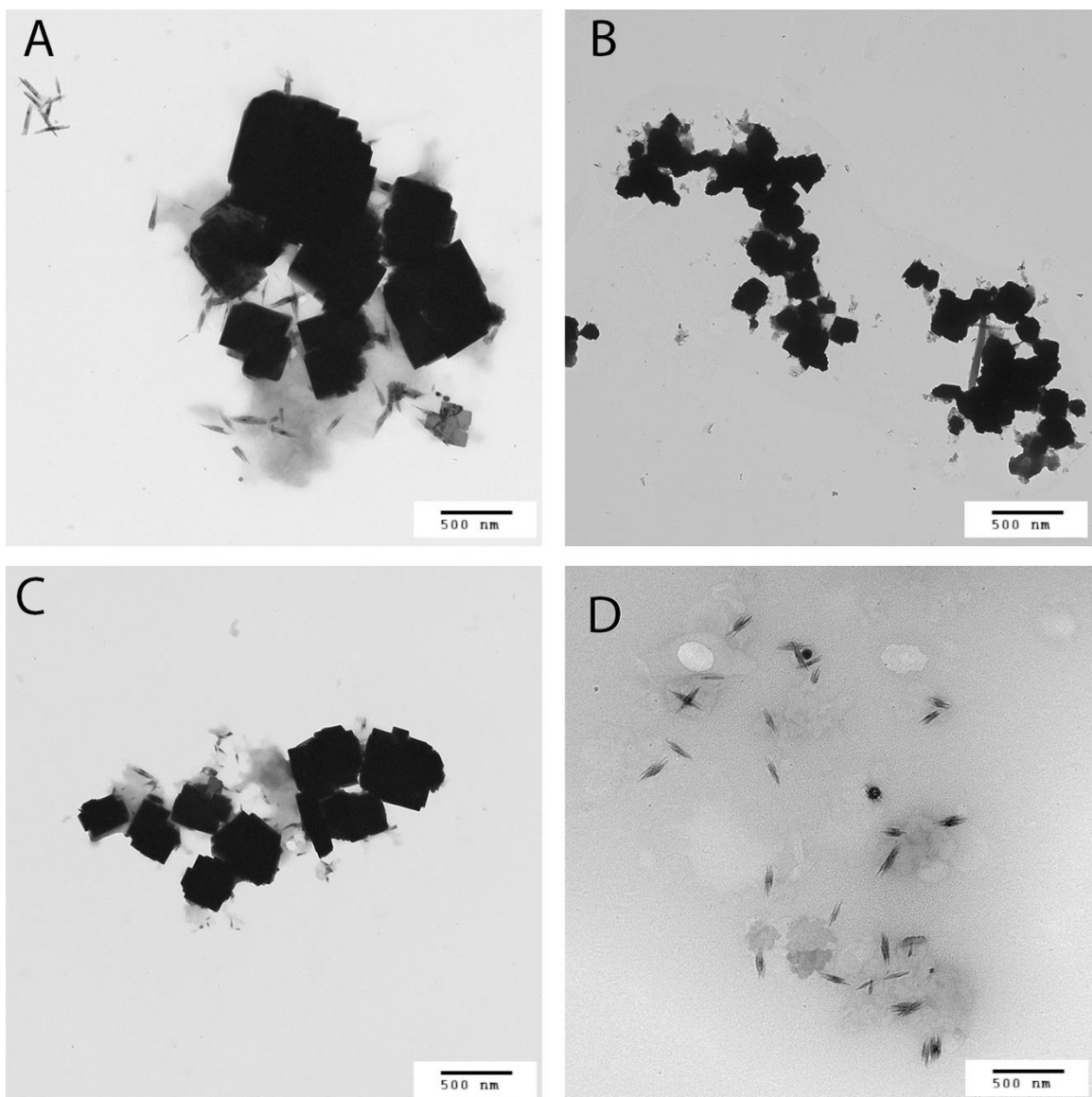


Figure S3. TEM characterization of LEM-TeNPs when 100 mM (A), 75 mM (B), 50 mM (C) and 25 mM (D) Te-precursor solution concentration was used.

For LIM-TeNPs, cubic-shaped nanostructures were found, with a size-metallic salt concentration dependence (Figure S3). For the lowest concentration, no cubic structures were found, while some nanorod-like structures were observed.

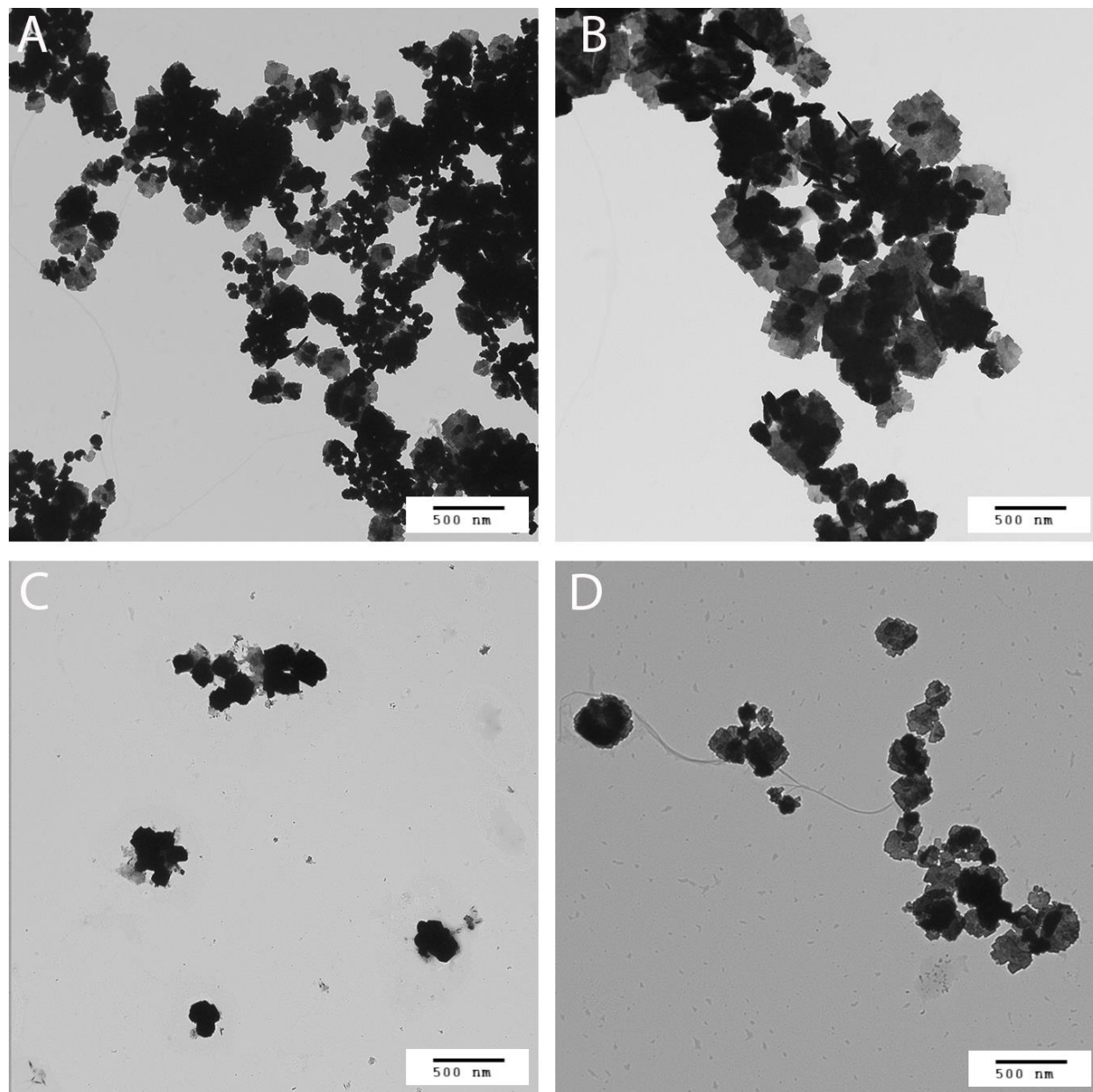


Figure S4. TEM characterization of LIM-TeNPs when 100 mM (A), 75 mM (B), 50 mM (C) and 25 mM (D) Te-precursor solution concentration was used.

For LIM-TeNPs, cubic-shaped nanostructures were found, with some agglomerates for the highest Te-precursor solution concentrations (Figure S4). The agglomeration decreases when the metallic salt concentration is lowered. The presence of some nanorods together with the cubic-like structures were noticed.

EDX characterization

Different areas of each sample were analyzed in order to assess the substances present in the nanostructures. The characterization confirmed that the electron-dense nanoparticles were composed of tellurium as proven by the presence of specific tellurium peaks in all samples. For OR-TeNPs (Figure S5), the analysis indicated the presence a single kind of nanostructures, Te nanorods, surrounded by a matrix composed mainly of carbon, oxygen, sodium and potassium.

As the ratio between the oxygen content and the carbon content is almost the same in area 1, with lots of nanorods, and in area 2, with mainly organic coating, we can infer that the nanorods are mainly composed of metallic Te. For LEM- and LIM-TeNPs (Figures S6 and S7, respectively), analysis of the different positions corroborated the presence of two tellurium structures, small tellurium nanoparticles, visible in the back-scattered electrons SEM images, and bigger cubic-shape crystals. In all samples, significant oxygen, carbon and sodium peaks were also identified, indicating the presence of a matrix embedding the nanostructures coming from the citric extract and the salt used in the synthesis process. Focusing our attention in Fig. S6 corresponding to LEM-Te NPs, the ratio oxygen(atomic%)/carbon(atomic %) in Spot 1, on top of a big cubic-shape crystal, is four times higher than that in Area 2 without big crystal, which indicates that the big crystal contains a significant amount of oxygen. Thus, such a higher content of oxygen suggests partial oxidation of the tellurium core, in agreement with the XRD

patterns (Figure 3 in the main manuscript). A similar case is deduced from Figure S7 corresponding to LIM-Te NPs. Finally, potassium, magnesium and calcium species were also found in all the spectra and it has been hypothesized that their presence may be derived from the orange, lemon and lime themselves, as well as from the metallic salt (sodium-containing tellurite). As described in the literature, citric juices contain a good amount of potassium¹, being the metal in highest content, with values between 15 and 300 mg/L. The detected silicon amount came from the use of Si substrates for the sample deposition.

OR-Te NPs

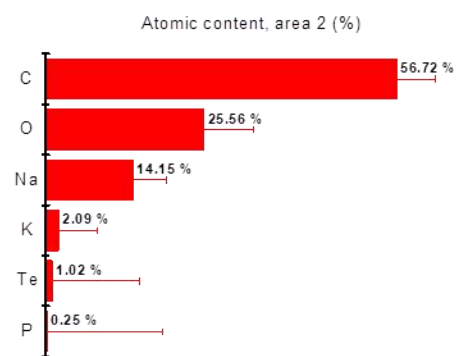
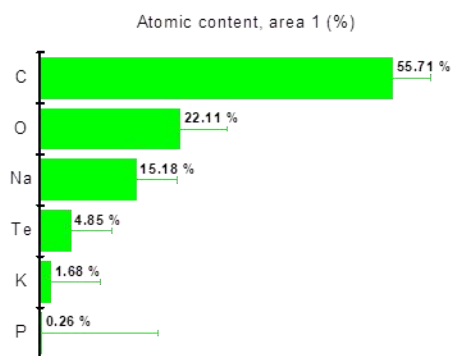
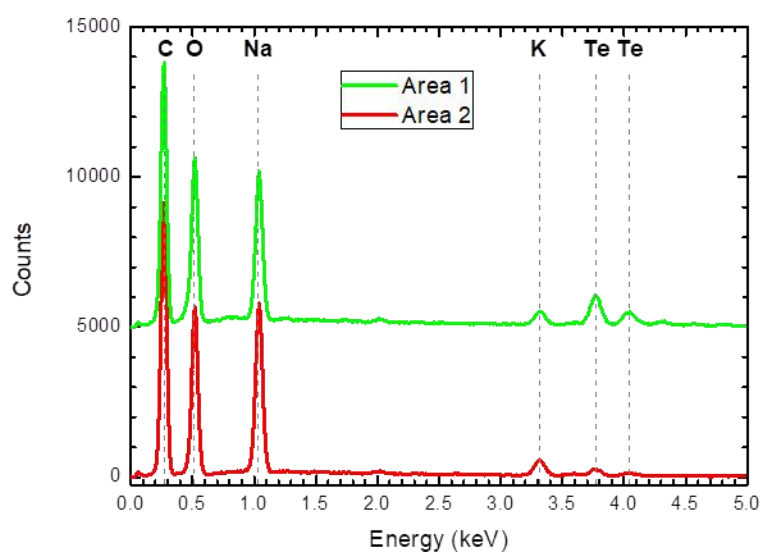
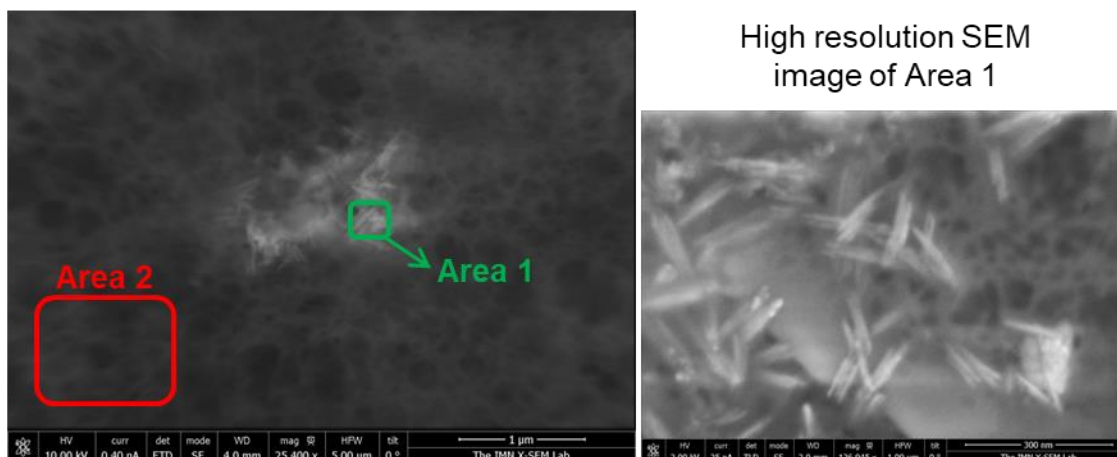


Figure S5. EDX characterization of OR-TeNPs, showing the presence of tellurium within the sample, as well as carbon, oxygen and sodium. The spectra were taken in different zones: Area 1 corresponds to the tellurium nanorods embedded in an organic matrix, and Area 2 corresponds to the surrounding matrix with some buried nanostructures not observed in the image (some tellurium is also detected there).

LEM-Te NPs

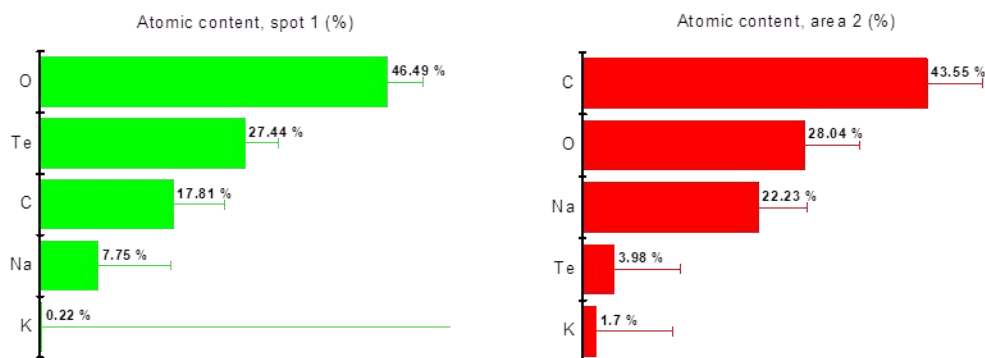
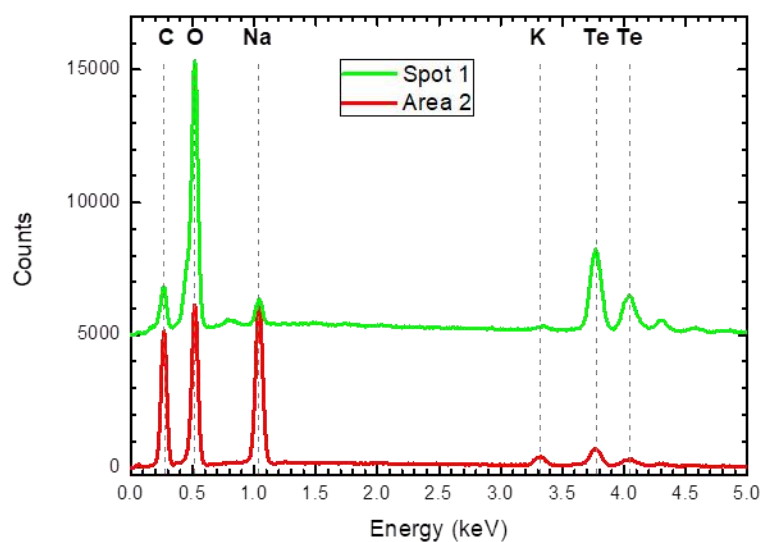
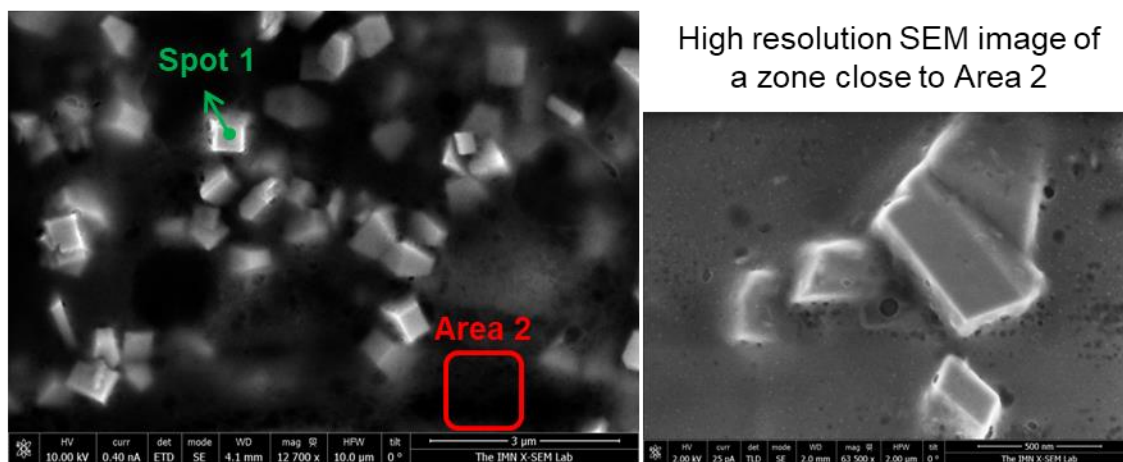


Figure S6. EDX characterization of LEM-TeNPs, showing the presence of tellurium within the sample, as well as carbon, oxygen and sodium. The spectra were taken in different zones: Spot 1 corresponds to one of the big tellurium crystals found in the sample and Area 2 corresponds to the surrounding organic matter, where the small dispersed nanoparticles are confirmed to be made of tellurium.

LIM-Te NPs

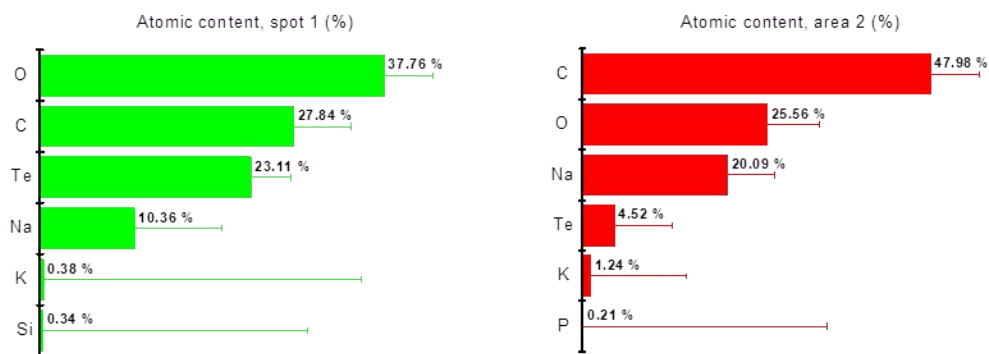
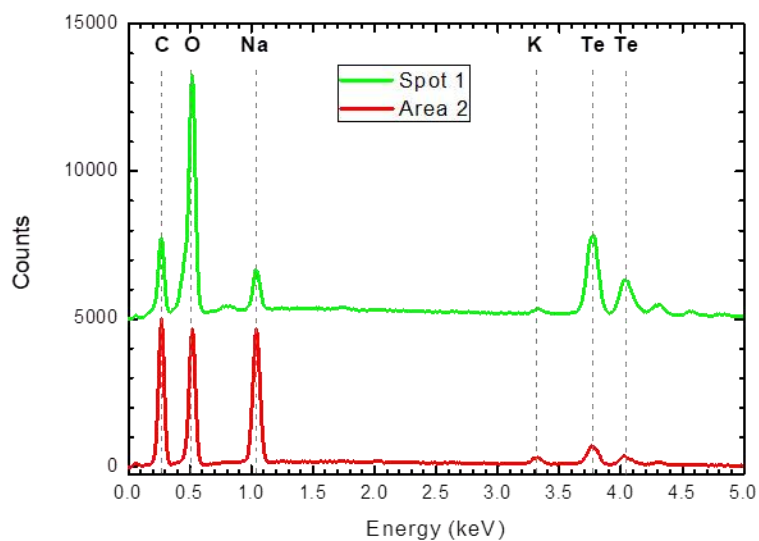
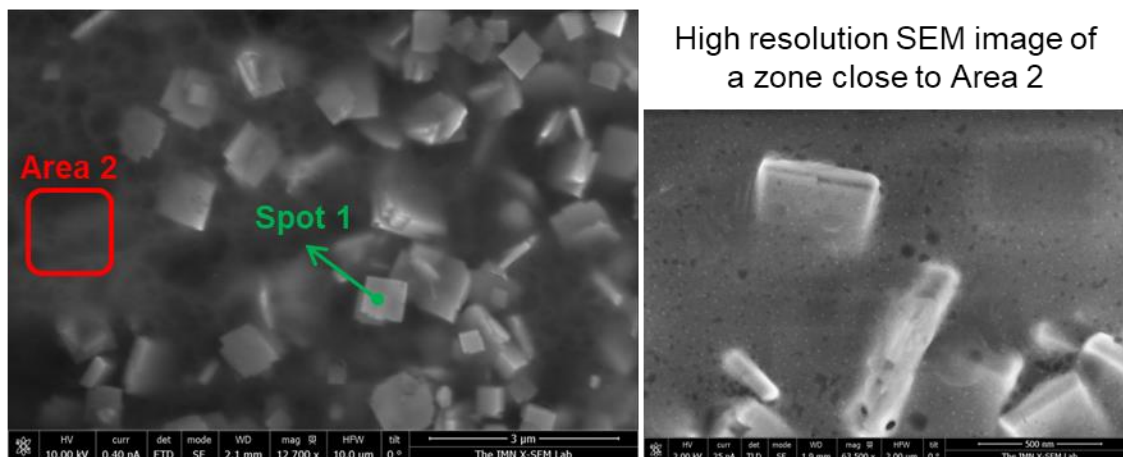


Figure S7. EDX characterization of LIM-TeNPs, showing the presence of tellurium within the sample, as well as carbon, oxygen and sodium. The spectra were taken in different zones: Spot 1 corresponds to one of the cubic tellurium crystals found in the sample and Area 2 corresponds to the surrounding organic matter, where the small dispersed nanoparticles are confirmed to be made of tellurium.

XRD characterization

XRD patterns are shown in Figure 3 in the main manuscript. The lattice parameters calculated for OR-TeNPs and the orthorhombic LEM-TeNPs and LIM-TeNPs are also reported in Table S1.

*Table S1. Lattice parameters calculated for Orange-TeNPs (*h*-Te) and, Lemon-TeNPs and Lime-TeNPs (β -TeO₂)*

Sample	<i>a</i> / Å	<i>b</i> / Å	<i>c</i> / Å
OR-TeNPs	4.476	4.476	5.856
<i>h</i> -Te ²	4.456	4.456	5.921
LEM-TeNPs	12.019	5.419	5.546
LIM-TeNPs	12.045	5.434	5.547
β -TeO ₂ ³	12.035	5.464	5.607

XPS analysis

Figure 4 in the main manuscript presents the wide energy range scan of the Te nanoparticles obtained from the orange, lime and lemon juices using XPS analysis. Quantification is reported in Table S2. A comparison of the three samples evidenced that the higher Te concentration was detected in the lemon dispersion, which doubled the orange one.

Table S2. Composition of the samples extracted from the wide energy range scans displayed in Figure S8.

	Composition at%				
	C	N	Na	O	Te
OR-TeNPs	59.2	1.7	1.0	37.7	0.4
LIM-TeNPs	65.0	1.1	0.6	32.6	0.6
LEM-TeNPs	62.5	1.1	1.2	34.4	0.8

Detailed analysis of the core level peaks enabled the observation of certain differences between the samples. Figure S8 (left) presents the Te 3d core level peak of the samples. Two components are present in the Te 3d; the first component at 573 ± 0.1 eV corresponds to the metallic component of Te $3d_{5/2}$ and the other component at 576 ± 0.2 eV, corresponds to the oxidized component^{4,5}. . By having a look to the proportion between the metallic and the oxidized components (Table S3), LEM-TeNPs - the samples with higher metallic Te proportion – only presented a 6 at% of Te oxidized, whereas the amount of oxidized Te is 18 at% in OR-TeNPs. The difference between these results and those obtained with the other techniques (EDX, XRD) is due to the inherent characteristics of the technique: XPS is a surface analysis technique where the average depth of analysis for a XPS measurement is only a few nm, much smaller than the penetration depth in the measurements by EDX and XRD.

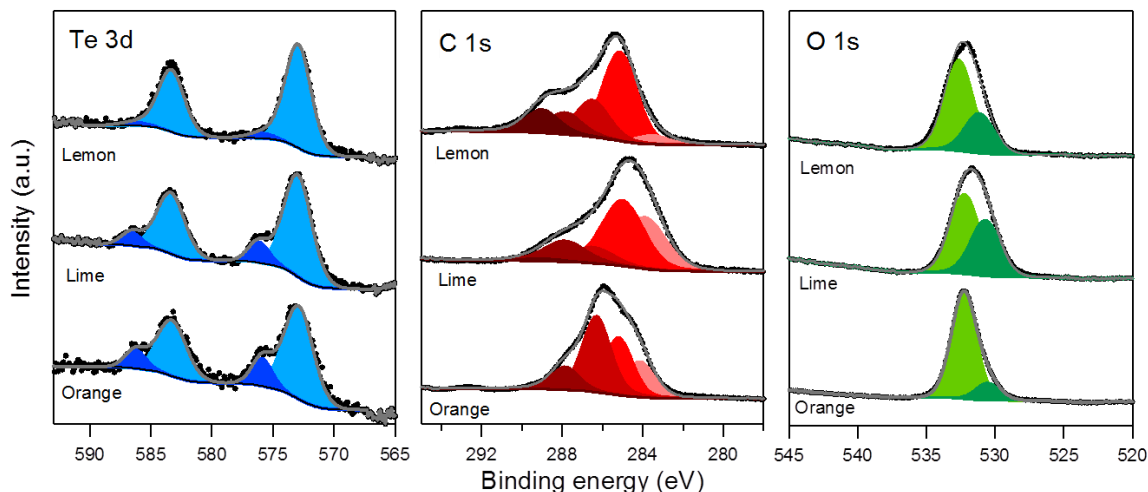


Figure S8. XPS Core level spectra of Te 3d (left), C 1s (center) and O 1s (right) of OR-, LEM- and LIM-TeNPs, respectively.

Besides, the analysis of the C 1s core level spectra of the samples revealed significant differences between the samples (Figure S8 (center)). Five components were used for the fitting, all of them were forced to have the same full width at half maximum (FWHM). These components corresponded to C-C/C-H bonds at 285 ± 0.2 eV; C-O / C-N bonds at 286.3 ± 0.2 eV; C=O bonds at 288.1 ± 0.2 eV and O-C=O bonds at 289 ± 0.2 eV. These four components are typical from organic compounds⁶. The fifth component that appeared at a lower binding energy (284 ± 0.2 eV) can be attributed to carbon in the sp^2 configuration⁷. The relative intensity of each component varies depending on the sample. Table S3 displays the proportion of each component of the C 1s and O 1s. OR-TeNPs – the one with the highest amount of oxygen – is the only sample in which the main component of the C 1s is not the C-C bond, and the C-O contribution is the most abundant. In the three samples, the C=O contribution is similar (around 13 at%). Only in the lemon sample, the O-C=O contribution is representative and reaches 13 at%.

The O 1s core level of the samples can be fitted into two components, one at 532.3 ± 0.2 eV and another less intense at 530.8 ± 0.2 eV (Figure S8 (right)). The first component is in the energy range characteristic of carbon-oxygen bonds in organic compounds⁶. The second component is close to the energy range of Te oxide [NIST database <https://srdata.nist.gov/xps/>] although by having a look to the amount of Te oxide of each sample (Table S3), it is clear that there are also other contributions to this component. The elements present in small amounts (i.e., N, Na, Cu) can also contribute to this component when bonded to oxygen.

Table S3. Components used for the fitting of the C 1s and O 1s core levels.

	Te	TeO _x	C-C	C-O	C=O	O-C=O	sp ²	O1	O2
OR-TeNPs	82	18	30	41	12	0	17	83	17
LIM-TeNPs	86	14	42	11	14	2	31	59	41
LEM-TeNPs	94	6	49	21	13	13	5	70	30

Stability analysis

In order to verify the stability of the citrics-mediated Te nanoparticles synthesized using a metal precursor concentration of 50 mM, TEM imaging on the samples after 60 days of synthesis were carried out (Figure S9). In general, it is evident that the samples kept their original morphologies and features. For example, the 60-days old OR-TeNPs sample is composed of partial agglomerated thin nanoneedles (50-200 nm length and 2-15 nm wide), as seen in Figure S9A. These features are in accordance with the freshly synthesized OR-TeNPs sample (Figures 1A in main manuscript and S2C). In the case of 60-days old LEM- and LIM-TeNPs samples, agglomerated nanocubes with 100-200 nm in length were observed (Figures S9B and S9D,

respectively), which is in agreement with their corresponding initial samples (Figures 1B and 1C in the main manuscript, respectively).

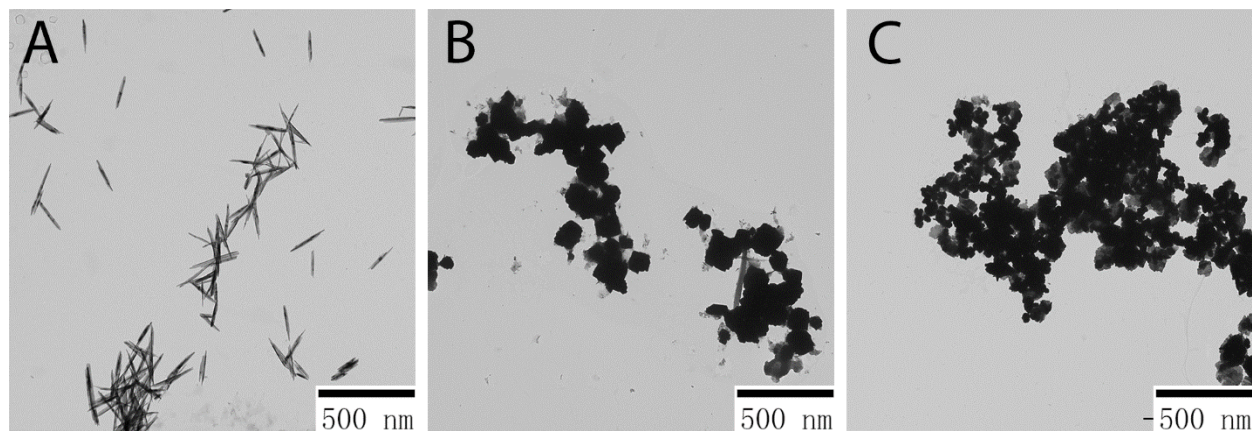


Figure S9. TEM images of OR- (A), LEM- (B) and LIM- (C) TeNPs after 60 days of synthesis. The samples were synthesized using a Te precursor concentration of 50 mM.

The stability analysis through the measurement of the Z-potential of the freshly synthesized and 60-days old Te-based nanoparticle colloids were also carried out. In general, a colloid or suspension is considered stable if the Z -potential is above a critical value of ± 30 mV⁸. Given the measured Z -potential values for the colloids OR-, LEM- and LIM-TeNPs (freshly and 60-days old samples, see Table S4), they can be considered stable.

Table S4. Zeta-potential values for freshly and 60-days old OR-, LEM- and LIM-TeNPs. The pH of the colloids were 7.0 ± 0.2

Type of NP	Z-potential (mV)	
	As-synthesized	60 days-old
OR-TeNPs	-27.06 ± 0.28	-29.11 ± 0.09
LEM-TeNPs	-23.66 ± 0.98	-26.12 ± 1.01
LIM-TeNPs	-30.18 ± 1.84	-28.39 ± 2.2

Antimicrobial activity of TeNPs

The antimicrobial activity of the different Te nanostructures was evaluated using 24-hours growth curve analysis, with results are displayed in Figure S10.

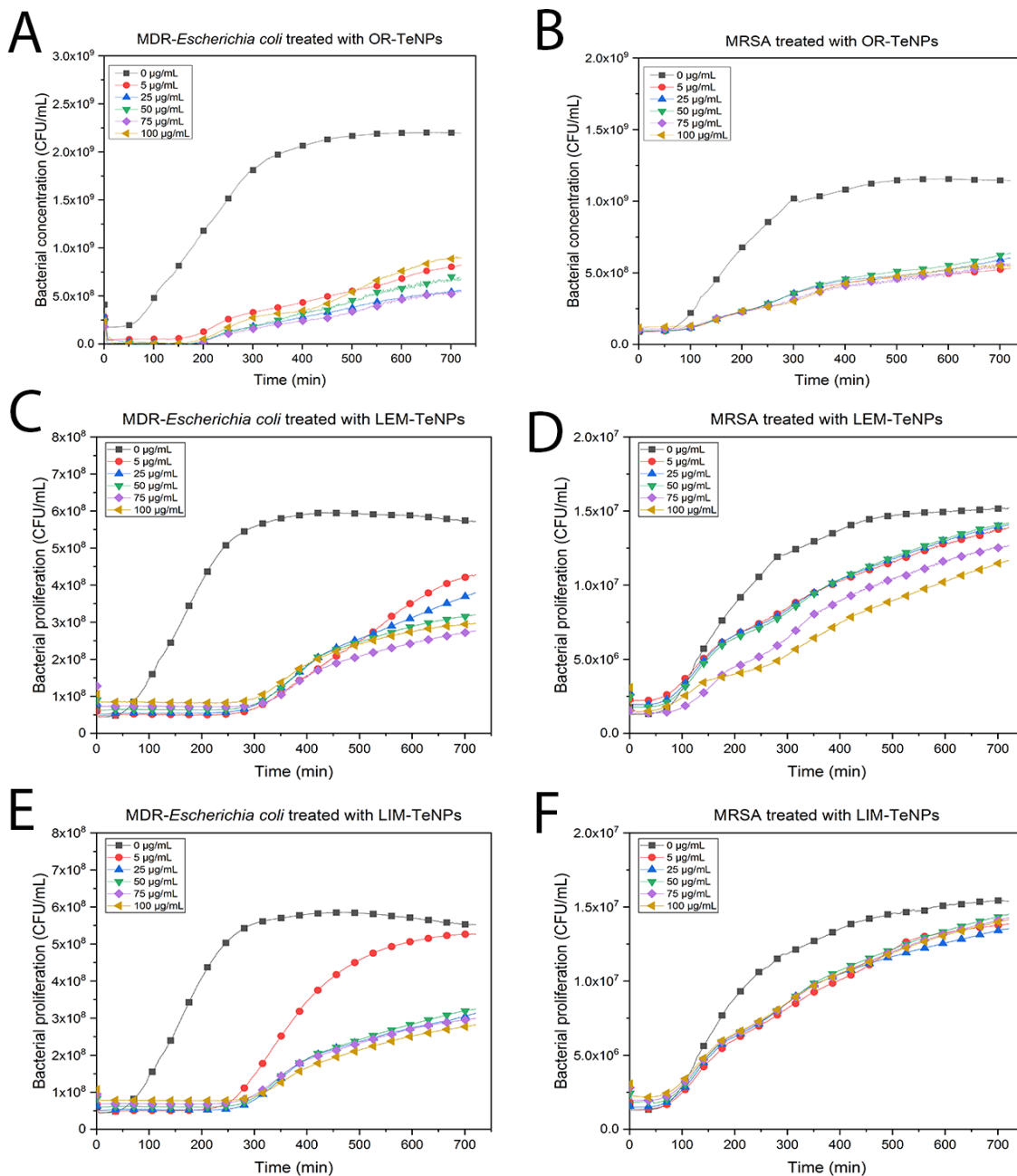


Figure S10. Citric-mediated TeNPs decrease the growth of *Escherichia coli* (A, C, E) and *Staphylococcus aureus* (B, D, F). Growth of a 10^6 CFU mL⁻¹ suspension of *Escherichia coli* (MDR-*E. coli*) and *Staphylococcus aureus* (MRSA) over 24 h in presence of different concentrations of tellurium nanoparticles. Data = mean \pm SEM, N = 3.

The parameters in the Gompertz equation were calculated and plotted for analysis for the three Te nanosystems. The parameter A represents the maximum specific growth of the bacteria under experimental conditions. Upon analysis of this parameter, it was found that a larger Te nanoparticle concentration led to lower asymptotic absorbance values (Figure S11A and S11B). The antibacterial activity was especially noticeable in the case of MDR *E. coli* (Figure S11A). The bigger decay in asymptotic absorbance was found in the treatment with these bacteria. In general, the OR-TeNPs displayed an antibacterial effect for both Gram-positive and -negative bacteria.

The maximum value of growth speed by the bacteria was analyzed using the parameter μ (Figures S11C and S11D). The plots demonstrated that larger TeNP concentrations resulted in lower maximum values reached for the bacteria; again, this was especially visible in the experiments with MDR *Escherichia coli* (Figure S11C). Finally, the parameter λ that represents the lag time in the bacterial growth under experimental conditions was analyzed, and results are shown in Figure S11E and S11F. Results showed that a higher TeNP concentration led to a shorter lag phase for bacterial growth. This was especially visible in the experiments with MDR *Escherichia coli* (Figure S11E), however, this trend was less obvious in the experiments with MRSA (Figure S11F). Since the lag phase refers to the point where bacteria are adapting themselves to the growth conditions offered by the media with nanoparticles, the delay may mean that the nanoparticles delay the maturing of bacteria, which are then unable to proliferate the way they should. The presence of nanoparticles may affect the bacterial growth cycle through the synthesis of RNA, enzymes or other molecules involved in this phase, which will need to be assessed in future studies.

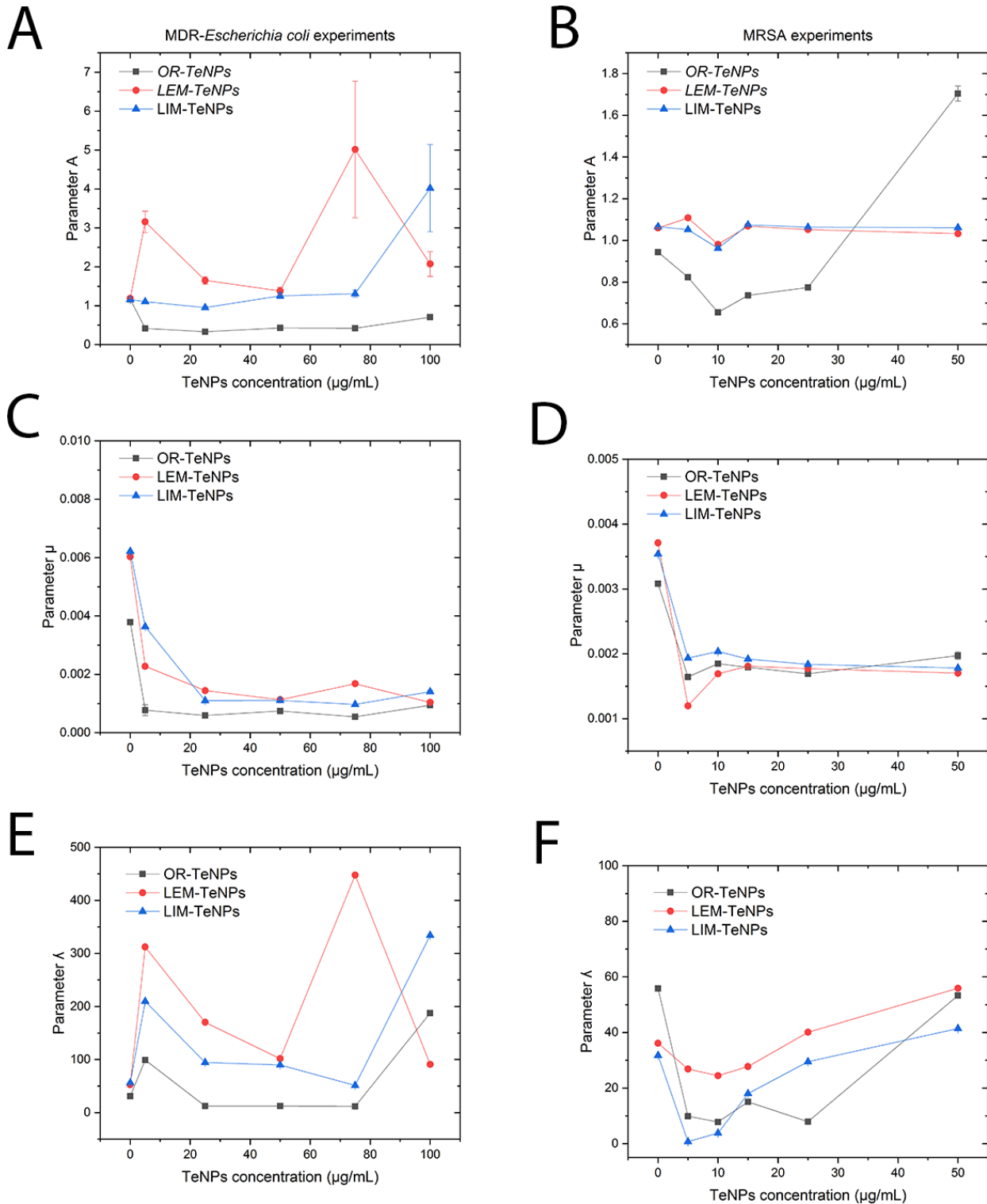


Figure S11. Gompertz parameters evaluation. The Gompertz parameters have been evaluated for the different nanoparticles (OR-, LEM- and LIM-TeNPs) in experiments with *Escherichia coli* (A,C,E) and *Staphylococcus aureus* (B,D,F). Data = mean +/- SEM.

References

- (1) D'Elia, L.; Barba, G.; Cappuccio, F. P.; Strazzullo, P. Potassium Intake, Stroke, and Cardiovascular Disease. *J. Am. Coll. Cardiol.* **2011**, *57* (10), 1210–1219.
<https://doi.org/10.1016/j.jacc.2010.09.070>.
- (2) Adenis, C.; Langer, V.; Lindqvist, O. Reinvestigation of the Structure of Tellurium. *Acta Crystallogr. Sect. C Cryst. Struct. Commun.* **1989**, *45* (6), 941–942.
<https://doi.org/10.1107/S0108270188014453>.
- (3) Beyer, H. Verfeinerung Der Kristallstruktur von Tellurit, Dem Rhomischen TeO₂. *Zeitschrift fur Krist.* **1967**, *124*, 228–237.
- (4) Beamson, G.; Briggs, D. High Resolution XPS of Organic Polymers: The Scienta ESCA300 Database. *J. Chem. Educ.* **1993**, *70* (1), A25.
<https://doi.org/10.1021/ed070pA25.5>.
- (5) Nevshupa, R.; Martínez, L.; Álvarez, L.; López, M. F.; Huttel, Y.; Méndez, J.; Román, E. Influence of Thermal Ageing on Surface Degradation of Ethylene-Propylene-Diene Elastomer. *J. Appl. Polym. Sci.* **2011**, *119* (1), 242–251.
<https://doi.org/10.1002/app.32519>.
- (6) Briggs, D. Handbook of X-Ray Photoelectron Spectroscopy C. D. Wanger, W. M. Riggs, L. E. Davis, J. F. Moulder and G. E. Muilenberg Perkin-Elmer Corp., Physical Electronics Division, Eden Prairie, Minnesota, USA, 1979. 190 Pp. \$195. *Surf. Interface Anal.* **1981**, *3* (4), v–v. <https://doi.org/10.1002/sia.740030412>.
- (7) Silva, R. R.; Mejia, H. A. G.; Ribeiro, S. J. L.; Shrestha, L. K.; Ariga, K.; Oliveira Jr., O. N.; Camargo, V. R.; Maia, L. J. Q.; Araújo, C. B.; Silva, R. R.; et al. Facile Synthesis of Tellurium Nanowires and Study of Their Third-Order Nonlinear Optical Properties. *J.*

Braz. Chem. Soc. **2016**, 28 (1), 58–67. <https://doi.org/10.5935/0103-5053.20160145>.

- (8) Liu, J.; Liang, C.; Zhu, X.; Lin, Y.; Zhang, H.; Wu, S. Understanding the Solvent Molecules Induced Spontaneous Growth of Uncapped Tellurium Nanoparticles. *Sci. Rep.* **2016**, 6, 32631. <https://doi.org/10.1038/srep32631>.